REPORT DOCUMENTATION PAGE

Form Approved
OMB NO. 0704-0188

1. AGENCY USE ONLY (Leave Blank)	2. REPORT DATE April 23, 2004	3. REPORT TYPE AND DATES COVERED Final Progress Report 25 September 25 1998 – January 24, 2004

4. TITLE AND SUBTITLE Experimental Study of Plasma/Propellant Interactions	5. FUNDING NUMBERS DAAG55-98-1-0519

6. AUTHOR(S)
Stefan T. Thynell and Thomas A. Litzinger

7. PERFORMING ORGANIZATION NAME(S) AND ADDRESS(ES) Department of Mechanical and Nuclear Engineering The Pennsylvania State University University Park, PA 16802	8. PERFORMING ORGANIZATION REPORT NUMBER None

9. SPONSORING / MONITORING AGENCY NAME(S) AND ADDRESS(ES) U. S. Army Research Office P.O. Box 12211 Research Triangle Park, NC 27709-2211	10. SPONSORING / MONITORING AGENCY REPORT NUMBER 39074-EG

12 a. DISTRIBUTION / AVAILABILITY STATEMENT Approved for public release; distribution is unlimited.	12 b. DISTRIBUTION CODE

13. ABSTRACT (Maximum 200 words)

The overall objective of the project was to improve our understanding of the various chemical and physical processes that occur during ignition by the plasma igniter. During the project period, electrical circuits, experimental setups were designed and manufactured, as well as data acquisition systems were acquired. The following primary findings have been obtained from this project: 1) to achieve ignition, a closed chamber configuration is needed, 2) JA2 propellant is readily ignitable, whereas nitramine-composite propellants show a two-stage mass generation behavior, 3) recovered samples from JA2 show changes in surface and sub-surface structure, in-depth melting, vaporization and chemical reactions, 4) recombination rates among plasma species are high, resulting in measurement of hydrocarbons at the surface having molecular weights from 1 to about 30 (H, H_2, C, CH, CH_2, etc.) and primarily NO, HCO and H_2CO from propellants, 5) the radiative heat flux reaches a maximum when the electrical power conversion reaches a maximum, 6) the UV component is significant, and 7) the near-surface emission from the plasma is significantly reduced compared to peak values due to plasma expansion and to rapid heat losses by radiation.

14. SUBJECT TERMS Plasma-propellant interactions, ignition of solid propellant, pressure measurements, high-speed film camera, high-speed CCD camera, JA2, XM39, and M43 propellants, ignition delay, fast-response heat flux gauges, radiative heat flux		15. NUMBER OF PAGES 31
		16. PRICE CODE

17. SECURITY CLASSIFICATION OR REPORT UNCLASSIFIED	18. SECURITY CLASSIFICATION ON THIS PAGE UNCLASSIFIED	19. SECURITY CLASSIFICATION OF ABSTRACT UNCLASSIFIED	20. LIMITATION OF ABSTRACT UL

TABLE OF CONTENTS

1 SUMMARY OF PROBLEM STUDIED

The electro-thermal-chemical (ETC) propulsion concept has been the subject of substantial research activities related to potential application in medium and large caliber weapons systems. The reason for this is that introducing the ETC plasma as an ignition source has revealed several attractive benefits over conventional igniter systems, such as shorter ignition delay[1], reduced temperature sensitivity of the propellant[2,3,4], better controlled propellant mass generation rates[5], and reduced susceptibility to anomalous ignition transients, and thus an enhancement of the safety of personnel. All of these have a significant effect on the ballistic behavior of ETC gun systems so as to improve gun performance. However, a complete understanding of the mechanical, physical and chemical mechanisms underlying the plasma propellant interaction is needed in order to effectively exploit the ETC igniters.

The ETC plasma is formed within a hydrocarbon capillary. During the rapid capacitive discharge process, electrical energy is converted into various other forms, including internal, kinetic and chemical energies, with substantial ablation heat transfer to the capillary's wall. The sub-millisecond duration of the electrical discharge is achieved through selection of the electrical circuit components, generally consisting of a capacitor, an inductor, and the plasma within the capillary representing the resistor. As a result of the rapid discharge in the very small volume of the capillary, extremely high temperatures and pressures are established. Such a rapid discharge is achieved by using a thin trigger wire within the capillary that allows a highly efficient initiation and establishment of the plasma. The wire provides the initial electrical connection between the anode and cathode. The electrical circuit behavior, the trigger wire explosion phenomenon, as well as the fluid mechanics of the plasma propagation into a stagnant atmosphere are fairly well understood. However, many other aspects are much less understood, such as the underlying causes for the measured shorter ignition delay, enhanced burn rate during the electrical discharge process, and differences in the extent of the interaction between the plasma and various propellants.

From visualization studies with a single plasma jet propagating into stagnant air, it is clear that the flow field can be characterized as a classical under-expanded jet although the event is highly transient[6,7,8,9,10,11]. The plasma is formed during a rapid capacitive discharge, in which electrical energy is converted into various other forms, including internal, kinetic and chemical, within a confined volume whose boundary undergoes erosion. The sub-millisecond duration of the electrical discharge is achieved through a selection of the components of the electrical circuit, generally consisting of a capacitor, an inductor, and the plasma formation chamber, which represents the resistor. As a result of the rapid discharge, extremely high temperatures and pressures are established within the gas phase. Emission measurements indicate temperatures around 17,000 K in the gas phase upstream of the Mach disk[9]. Stagnation pressure measurements revealed peak values up to 5 MPa about 10 cm downstream of the nozzle exit[12].

Comprehensive modeling efforts are also being conducted[7,12], in which the ARL plasma code is used to compute the nozzle throat conditions based on the electrical power dissipation within the plasma chamber. The NRL Fast3D code is employed to simulate the plasma flow into the open, stagnant air. These transient calculations employ an axisymmetric grid. Comparisons with data acquired by White *et al*[6] show that pressure oscillations are captured, but the predictions are about a factor of 2 or 3 higher than those measured. It must be recognized that the employed model is being further refined to include species and chemical reactions in the gas phase.

2 OVERALL OBJECTIVES

The primary objective of the project was to gain insights from parametric studies that will contribute to the formulation of a more complete understanding of the various chemical and physical processes that occur during ignition by the plasma igniter. Another key objective was to provide data for validation of the models being developed at ARL.

2.1 Specific Experimental Objectives

1. Characterize species in the plasma jet and those produced in its interactions with propellants using the molecular beam mass spectrometer (MBMS) system.
2. Ascertain the local surface heat flux variations temporally and spatially.
3. Perform various parametric studies including:
    - Investigate the effects of plasma energy on ignition processes including ignition delay time.
    - Perform studies with propellants to determine the effects of propellant characteristics on interaction with the plasma.

3 METHOD OF APPROACH

3.1 Experimental Facilities

The diagnostic measurements largely fall into two aspects: characterization of plasma, and study of plasma-propellant interactions. Basically, these experiments were performed using two configurations, i.e., open-air and closed-chamber. The overall experimental setup illustrated in Figure 1 represents the open-air testing.
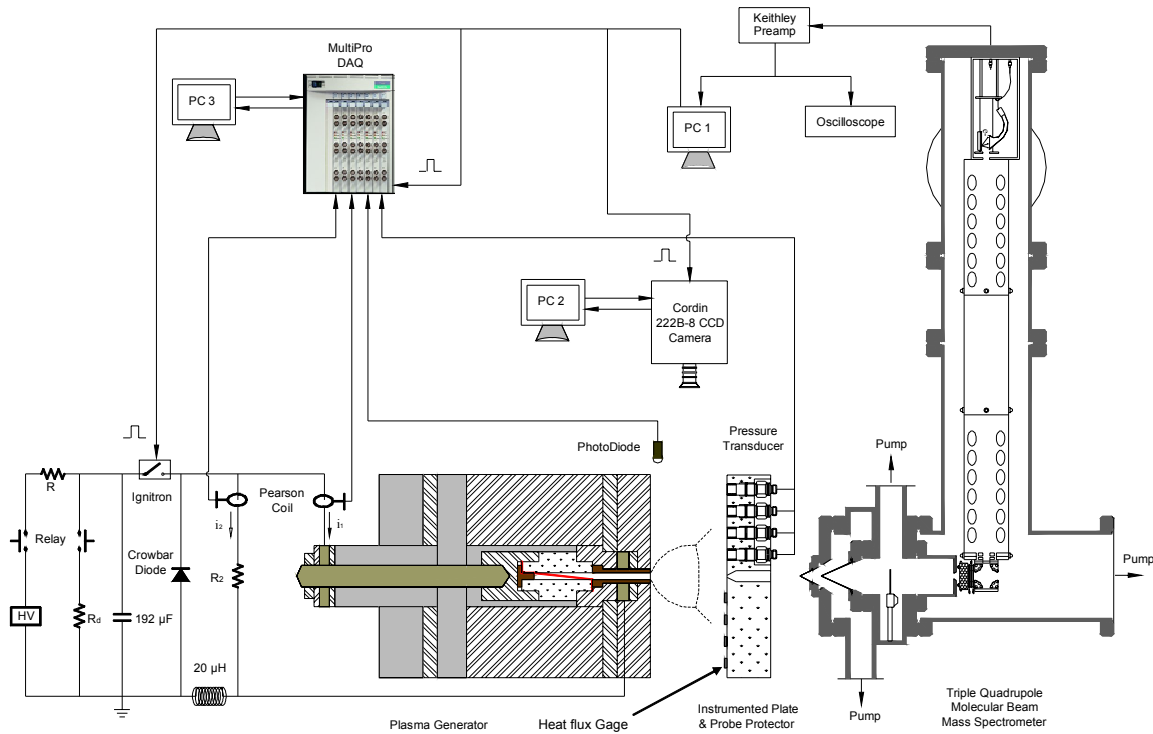
Figure 1 Overall experimental setup for PPI study.

The capillary plasma generation system includes the pulse-forming network (PFN) based on a resistance-inductance-capacitor (RLC) circuit, which is mainly comprised of an energy storage component that consists of two high-voltage fast-discharge capacitors connected in parallel to yield a total capacitance of 192 μF, pulse-shaping components including a 20 μH inductor, a crowbar diode, and a floating high-voltage mercury switch (ignitron) as the trigger unit. The capacitors can be charged up to 10 kV yielding maximum energy storage of 9.6 kJ. The plasma chamber consists of a capillary liner, a fine metallic wire, electrodes, and other conducting or non-conducting housing hardware. The capillary liner is typically made of either high-density polyethylene (PE, $[C_2H_4]_n$) or polycarbonate (Lexan, $[C_{16}H_{14}O_3]_n$), which is machined to have a bore length of 26 mm and a typical diameter of 3.2 mm. Located at each end of the capillary are two electrodes made of elkonite, a copper-tungsten alloy

(30% Cu, 70% W), which is resistant to material erosion. Typically, two twisted fine copper wires of 0.08 mm diameter, which run through the capillary and connect to the electrodes, serve as the discharge initiator. After being formed immediately upon triggering by the ignitron, the plasma flows through a nozzle that has dimensions of 3.2 mm (orifice diameter) and 26 mm (length) into open-air or a closed chamber. The nozzle is designed to have this length simply for accommodating to the dimensions of the plasma chamber.

In the open-air experimental setup, temporal variations in the local stagnation pressure were recorded at several positions as shown in Figure 1. Kistler 211B series pressure transducers were utilized for pressure measurements during open air testing. These transducers were mounted to a lexan support frame, and electrical insulation tape was used to prevent the transducers' sensing surfaces from being directly exposed to the charged particles in the plasma.

Heat flux measurements via thin films was utilized in efforts to gain an insight of how the ignition is achieved, and to understand the transient variation of radiative heat transfer. The principle of operation for the thin film heat flux gage is that a constant current flows through a thin metal layer whose resistivity depends on temperature, thereby measuring the voltage drop across the metal layer. Once the surface temperature of the film is known from the calibrated resistance versus temperature relationship, a mathematical approach can be utilized to deduce the heat flux data.

A Cordin 350 high-speed film camera with Fuji 160 color film was utilized for capturing images during the plasma evolution. This camera uses 35 mm film and is capable of acquiring up to 35,000 pictures per second with a 0.25 μs shutter speed. Each image measures 7 by 10 mm on the film, and a total of 224 images can be acquired for a film length of 867 mm. The negative of the film was scanned directly into a PC using a Nikon 2000 film scanner. In order to prevent the pictures from being over-exposed due to the extremely high luminosity of the plasma, two neutral density filters producing a total attenuation of 64 with a lens aperture of f/5.6 were selected for the framing speed of 35,000 pictures per second.

A Cordin model 222-8 gated, intensified CCD camera was also used. This camera is capable of acquiring 16 images, each with a pixel resolution of 1,300 by 1030, 10-bit gray scale, and exposure times down to 10 ns. The camera has 8 CCDs, and downloads the first set of eight images on a second set of CCD sensors. The first 8 images can be acquired at a framing rate of up to 100 million frames per seconds, that is followed with a delay of about 1 μs, and then a second set of 8 images at 100 million frames per second is acquired. A gain of up to 7,000 is available on each frame, which should enable sort exposure times even in moderate light conditions. However, the plasma is utterly bright, which implies that filters must be used with the CCD camera as well. With the short exposure time, the motion of the shock waves and luminous zones are effectively frozen, and the high pixel resolution yields a great detail of the acquired images. The images are directly downloaded to memory for storage and viewing, which simplifies the work significantly.

An Extrel triple quadrupole mass spectrometer (TQMS) system with a molecular beam sampling system was used for species measurements. The product gases are extracted by a sampling cone that has a 100 μm orifice and enter the first stage of pumping, which is supported by a 3000 L/s diffusion pump. The sample stream enters the second stage of pumping through a skimmer with a 1000 μm orifice; when needed the beam can be chopped to enhance signal to noise ratio. The molecular beam then enters a cross-beam ionizer that ionizes the gases by electron impact, and turns the ions ninety degrees to enter the quadrupole filters. When sampling is done from the plasma, plasma ions can be detected by turning off the ionizer and electrically biasing one or both of the skimmers.

The three quadrupole filters can be set to operate either in "daughter" mode or in "parent" mode to differentiate and identify species. In the parent mode of operation, the species with different molecular weights are readily identified by their unique mass to charge ratio (m/z). In the daughter mode of operation, the first quadrupole mass filter (Q1) selects the parent ions of the desired m/z and allows them

to pass into the second quadrupole (Q2) where they collide with argon molecules. In this process, the ions are fragmented into several daughter species due to collision-induced dissociation. The daughter ions are then analyzed in the third quadrupole filter (Q3) to identify the parent species present at the given m/z[13,14].

Three data acquisition systems were involved in this study. A Nicolet MultiPro 120/150 data acquisition system along with its ProView software was used for pressure, current, and heat flux measurements. Software was provided with the CCD camera to yield full control, including among others setting of exposure duration, interframe time, CCD gains, focusing adjustment, triggering the CCDs, and downloading the captured images to a PC for storage and editing. The third data acquisition and reduction system was developed by this group for species measurements with the mass spectrometer.

3.2 Test Chambers

The burning behaviors of JA2, M43, and XM39, when ignited by the plasma, were comparatively studied through the measurement of pressure in the closed-chamber testing. Ignition and combustion process of JA2 in closed-chamber conditions were studied through high-speed photography (using the CCD camera). Two closed chambers with different configurations were used in this experimental work. The first one has dimensions of 3.5 cm in length and 2.1 cm in diameter, corresponding to a net volume of 15.8 cm^3. An insert was used to allow variation in the chamber volume, and for tests conducted with this chamber, the actual volume was 6.5 cm^3.
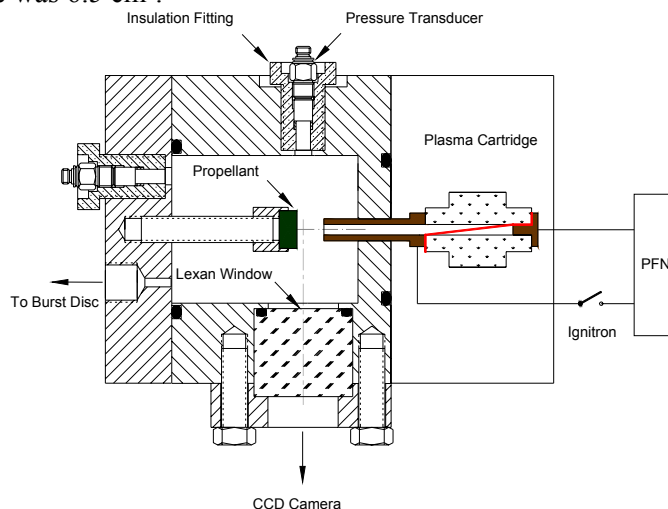

Figure 2 Windowed chamber for photography of PPI.

The second chamber is optically accessible (illustrated in Figure 2) to allow photography of propellant ignition and combustion processes. The windowed chamber measures 3.5 cm in length and 4.3 cm in diameter, yielding a net volume about 48 cm^3. The chamber is equipped with a 2.0 cm circular viewing port, and the optical window can withstand pressures up to 20 MPa.

In general, a sample holder, with one end screwed into the end plate of the closed chamber, brings the propellant sample close to the nozzle exit to enable normal exposure to the plasma jet. For tests with no propellant, an inert substitute having the same size with the propellant sample was used to maintain a same chamber volume. Two pressure transducers were mounted in different locations to allow simultaneous measurement of pressure time history in the chamber. A venting hole was connected to a solenoid valve for depressurization of the chamber as needed.

For closed chamber pressure measurements, a 211B1 model Kistler pressure transducer was used, which has a much higher measuring range of 0-10,000 psig and a maximum rise time of 1 μs. Protection

of the pressure transducer proved to be even more important in the closed-chamber testing, because, in addition to the electromagnetic effect of the plasma, thermal radiation from the plasma can easily damage the pressure transducer. Thus, in closed-chamber testing, recess-mounting was used to allow the sensing area of the pressure transducer to be covered by a thin layer (~ 1 mm) of vacuum grease, which was then covered by one strip of electrical insulation tape. A check with compressed air showed evidence that the grease layer and the tape allowed adequate rise time for the considered type of measurements.

3.3 Mass Spectrometry Studies

Information of species in the plasma-propellant interfacing region is very important to the understanding of possible chemical enhancement. Species measurement over this region proved to be very challenging. Direct measurement in closed-chamber configuration is desired, but the chance for the sampler to survive the harsh conditions in the closed chamber is quite small. The short time duration of the open-air plasma does not match the TQMS response. Additionally, since the plasma jet has a very low density, it is hard to detect any species within the jet with a relatively high intensity. These difficulties were overcome to some extent by a specially designed setup, which is shown in Figure 3.
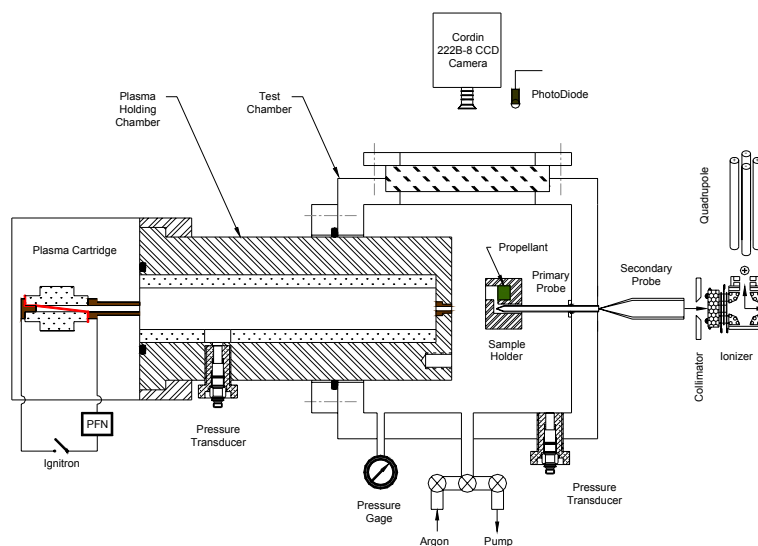

Figure 3. Setup for species measurement in a closed environment.

The plasma-holding chamber is a long cylindrical chamber with one end attached to the plasma generator and the other extending to a test chamber. A tubular sleeve of polyethylene or lexan was inserted in the holding chamber to vary its actual volume, and more importantly, to weaken the heat transfer from the plasma to chamber walls. On the bottom wall of the holding chamber is installed a small nozzle (1 ~ 2 mm I.D.) that uses elkonite to minimize material erosion. The test chamber, which interfaces with the mass spectrometer through the flange that holds the primary microprobe, has a 4×4×4 inch^3 internal volume and is equipped with a 2.6 inch circular window for photography. The plasma-holding chamber coupled with a closed test chamber was considered as a promising setup in that the holding chamber prolongs the sampling duration through sampling a secondary jet from it rather than the primary plasma jet from the plasma generator; the closed test chamber creates a sub-atmosphere condition by connecting to a vacuum pump; this sub-atm condition increases the absolute fraction of species from the secondary jet in the whole plume that entering the sampling probe. Also, since the holding chamber and test chamber were connected, it is very convenient to purge the chambers with any background gases of interest to investigate the effects of ambient conditions on the species information of the secondary jets or the plasma. The sample holder has a short passage that connects the propellant sample and the sampling probe tip. This special configuration was expected increase the likelihood of detecting the

species near the propellant surface. The sample holder was removed when species measurement was done with plasma alone.

3.4 Radiative Heat Flux Measurements

In order to better understand the role of radiative heat transfer, a thin-film sensor and circuitry were designed, manufactured and tested. The principle of its operation is that a constant current flows through a thin metal layer whose resistivity depends on temperature[15,16]. Once the surface temperature of the film is known from the calibrated resistance versus temperature relationship, an inverse technique is utilized to deduce the heat flux data corresponding to the temporal evolution of the measured surface temperature[17,18,19]. Since the film is thin and located on a poorly conducting substrate, the frequency response is high.
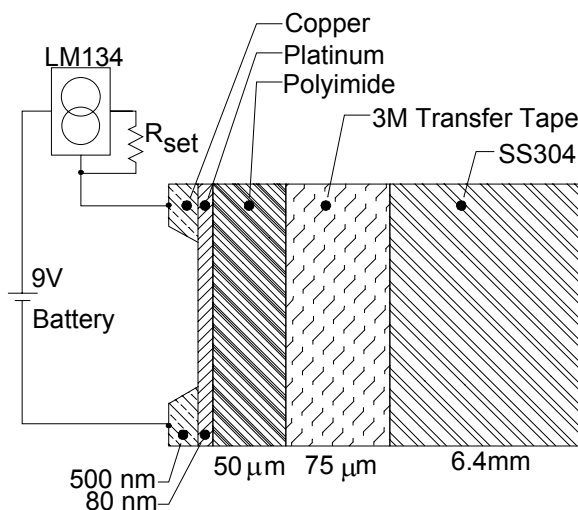

Figure 4. Layout of platinum thin film heat flux gage.

Figure 4 shows the basic design of the thin film heat flux gage. The polyimide layer, which is 50 μm thick has a low thermal conductivity (0.1 to 0.35 W/m K) and is stable under working temperatures of 250 to 320°C.[20] Sputtering has been employed to yield films that attach well to the polyimide substrate. The thickness of the sputtered metal is typically 80 nm, and its width and length are, respectively, 0.25 and 12 mm. The constant current source is National Semiconductor's LM 134 chip, powered by a low-noise 9V battery. The electrical leads are soldered onto the 3 mm wide copper film, to yield a high-strength and high-electrical conductivity connection.

Following the experiments by White *et al.*[21], various arrangements are needed in order to measure the heat flux from the plasma. The heat flux measurement is interfaced to the existing experimental setup. Each heat flux gage has two different configurations, as shown in Figure 5. One configuration corresponds to measurements at the location of the pressure gauges on the stagnation plate, to yield the maximum heat flux rates. The second configuration is below the plasma, in order to determine the extent of transmission by the fused silica window. This window is needed as the total heat flux rates are large (radiative, convective and heat release from recombination reactions). Furthermore, some ionic species remain at the surface and tend to produce significant electrical noise. The diodes are used to determine plasma emergence (left diode) and plasma arrival (right diode).
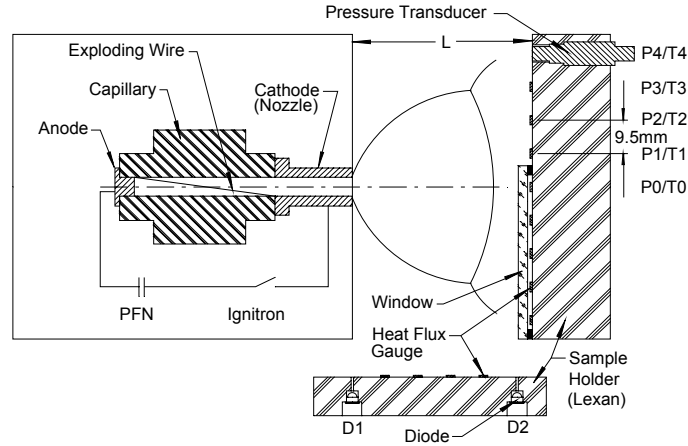
Figure 5. Setup of heat flux gauges on the stagnation plate and below the plasma.

4 DISCUSSION OF RESULTS

Results from this study are discussed in two parts: characterization of the capillary plasma and investigation of plasma-propellant interactions.

4.1 Characterization of Plasma

Various experiments were conducted to characterize the ETC plasma in several aspects, including electrical parameters, gas dynamics, recombined species, and radiative heat flux. Results from these studies will be summarized in the following sections.

4.1.1   Electrical Parameters

Figure 6 shows a typical result of the electrical variables during the capillary discharge. The power, energy and resistance traces were deduced from the measured current and voltage across the capillary. The general trends in these parameters are quite similar for all tests under a given condition. Discharge of the capacitor begins upon triggering the ignitron switch, and ohmic heating of the wire quickly increases the voltage across it and initiates a process of melting, fragmenting and vaporizing of the wire. The spikes appearing on resistance traces at early times represent the exploding process of the thin wire. The sharp peaks on the voltage trace, corresponding to the last spike on the resistance curve at 11 μs, indicates the completion of the wire explosion and the formation of an initial plasma, which enables electrical conductance of the circuit to continue. A small change of slope in the current profile occurs at this time due to the shift of conducting medium from the metallic wire to charged particles in the plasma.

As more energy input proceeds, ohmic heating increases the temperature of the initial plasma to a sufficiently high level to cause ablation of the capillary wall material (including the end electrode) due to the extremely high radiative fluxes. Vaporization and ionization of the ablated material then produce much more plasma, causing a sharp reduction in resistance. After this sharp decrease, the resistance continues to decrease more slowly and then eventually increases. The variation of resistance is an indication of change in electron number density and in the collision frequencies between electron and other particles. During the plasma discharge, the voltage across the capillary changes very little. Consequently, variation of the current is determined by the variation in the resistance. The current reaches a peak value of 12.7 kA at ~ 85 μs, after which it starts to decrease until the completion of discharge at ~ 280 μs, where the current decreases and the resistance increases. Most of the energy initially stored in the capacitor (2.40 kJ) is deposited in the plasma (2.36 kJ) and only a small portion (~ 1.6 %) is consumed in resistive losses, remains in the capacitor, or is dissipated in the bypass resistor. The power curve indicates that the electrical energy from the capacitor is discharged to the capillary plasma at varying rates, which reach a maximum of 19.2 MW at 77 μs, slightly earlier than the appearance of the peak current.
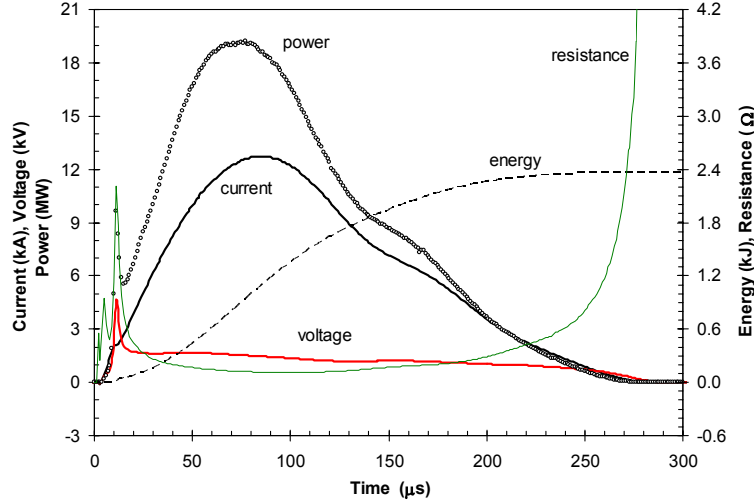
10

Figure 6. Typical electrical parameters of capillary plasma (3.2 mm capillary, charging at 5 kV).

Figure 7 shows the effect of bore diameter on the electrical discharge. As the diameter increases, the ablated mass increases, thereby increasing the total number of charge carriers within the plasma, and therefore decreasing the resistance of the plasma. Hence as the bore diameter is increased, a longer time period is required to convert the electrical energy into other forms of energies.
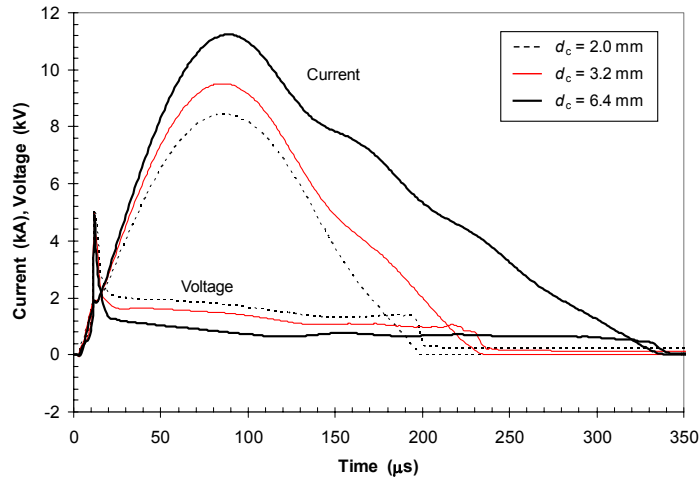

Figure 7. Dependence of capillary discharge on capillary bore size (charging at 4 kV).

4.1.2   Gas Dynamics

High-speed photography of the plasma evolution has been obtained over a range of ignition energies and distances between the plasma chamber and the stagnation plate. As an example, Figure 8 shows the evolving plasma jet. From these images, one can see the expected gas dynamic features characteristic of a highly under-expanded supersonic jet: a distinct barrel shock (oblique shock) and a strong Mach disk (normal shock). In the images, regions of greatest luminosity were found near the exit port and on the opposing plate just downstream of the Mach disk, which are expected to correspond to the highest temperature zones. The modeling work by ARL confirms these expectations[22].

As the jet impinges on the perpendicular plate, it is decelerated and redirected, producing a flow in the radial direction along the plate. The presence of the plate makes the plasma jet flow even more complex than the freely expanding plasma jets. As a result of interaction with the plate, the surface

pressure on the plate oscillates. The plasma image also shows what appears to be many small eddies surrounding the barrel shock. These eddies are believed to be caused by plasma mixing with air along the shear layer and may also involve chemical reaction of fuel-rich plasma species with air.
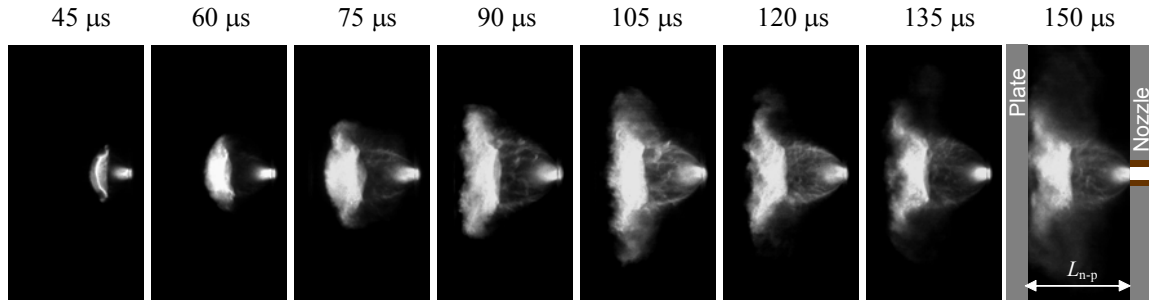

Figure 8. Evolving capillary plasma jet (6.4mm Lexan capillary, 4 kV, L_{n-p}=40mm).

Figure 9 gives another example of the effect of nozzle-plate spacing on the plasma jet flow. Interestingly, as the nozzle-plate spacing is reduced to a certain small value, the distinct multiple shock system that is present for a longer spacing is replaced by a "Swan-shaped" shock wave developing in the narrow space between the nozzle exit plane and the sample surface plane. This shock structure acts as if a physical plate much larger than the sample existed and confined the plasma within a 5 mm thick region.
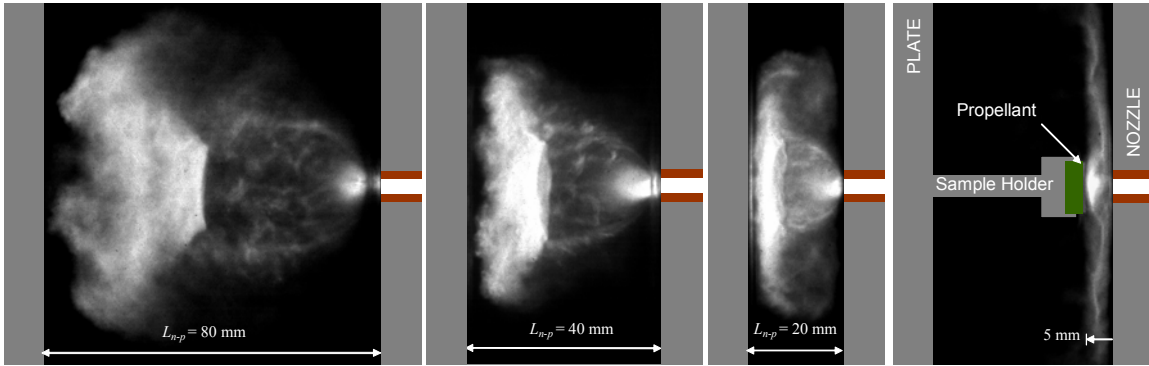

Figure 9 Capillary plasma jets at different nozzle-plate spacings (3.2mm capillary, 4kV)

A number of tests have also been conducted to obtain the pressure distribution along the stagnation plate, including studies to determine the effects of plasma energy and spacing between the plasma generator and the stagnation plate. Figure 10 shows stagnation pressure results for tests that were conducted with different nozzle-plate distances (L_{n-p}). These tests illustrate the effect of L_{n-p} on the surface pressure that a propellant sample would experience in normal impingement situations. The results of the tests give information on the transit time of the plasma jet as well as the timing at which the jet arrives at each transducer location.

In addition, information on peak pressures and variation of pressure due to complex wave motions in the flow field is captured. Significant oscillations in pressure are observed, which are reproduced well in modeling work by ARL, which confirms that such oscillations are physical in nature, being produced by the complex wave structures within the jet and their interaction with physical boundaries.[22] It is reasonable to expect that, when subject to such impingements from hot plasma jets (T > 10,000 K), the propellant will undergo mechanical changes caused by the resulting mechanical and thermal loads, and these changes could play an important role in the subsequent ignition and combustion. In addition, the use of photodiodes has established the time of the emergence of the plasma from the plasma chamber, thus providing useful data that are used for improving the model of the discharge process within the capillary.
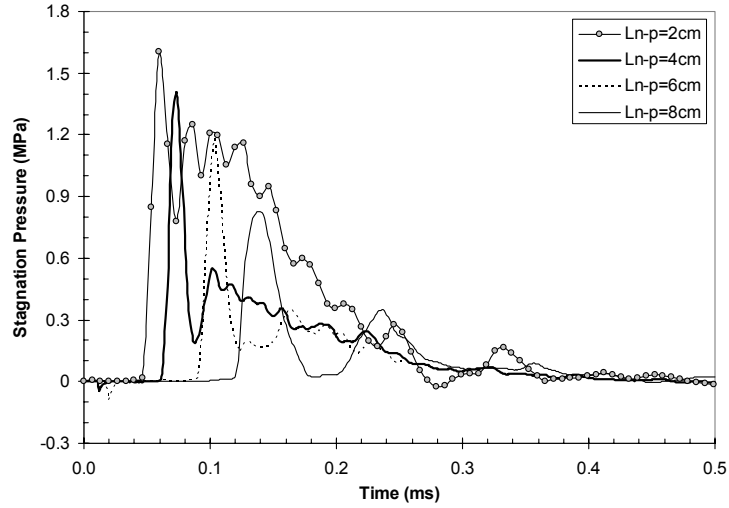
Figure 10. Surface pressures on the stagnation plate at various nozzle-plate spacings.

4.1.3 Species

Figure 11 presents two images showing the microprobe submerged in the jet for sampling species using the configuration illustrated in Figure 3. The duration of jet flow out of the holding chamber was substantially extended, typically around 50 ms, which is sufficiently long to match the response times of the mass spectrometer.
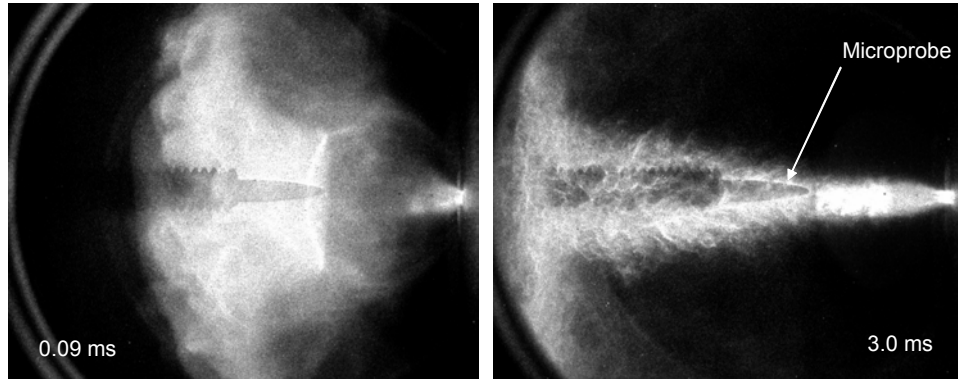

Figure 11 Microprobe sampling of the jet discharging from plasma-holding chamber.

As an example, Figure 12 displays the detected species as a result of recombination from the plasma species, i.e., C, H, C^+, H^+ and electron. The left plot shows three species of higher intensities, including C_2H_2, C_2H_3, and H_2. Other species having relatively low intensities are CH_4, H, CH_3 and NO, and they are plotted in the right graph.
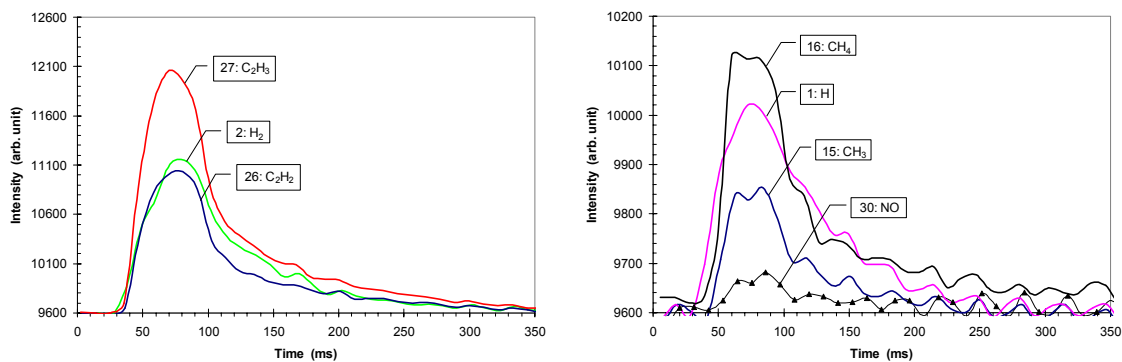
Figure 12. Recombined species from plasma: major (left) and minor (right).
Test conditions: 4kV, 3.2mm PE capillary, trigger plasma at 20ms.

A series of experiments were performed to investigate the effect of input electrical energy on the recombination reactions in the plasma, and the results were shown in Figure 13, where the intensity ratio of C_2H_2 over C_2H_3 were plotted against four charging levels. It reveals that an increase in charging levels increases this ratio, indicating that small radicals become increasingly dominant in the jet as more energy is deposited into the plasma, as expected.
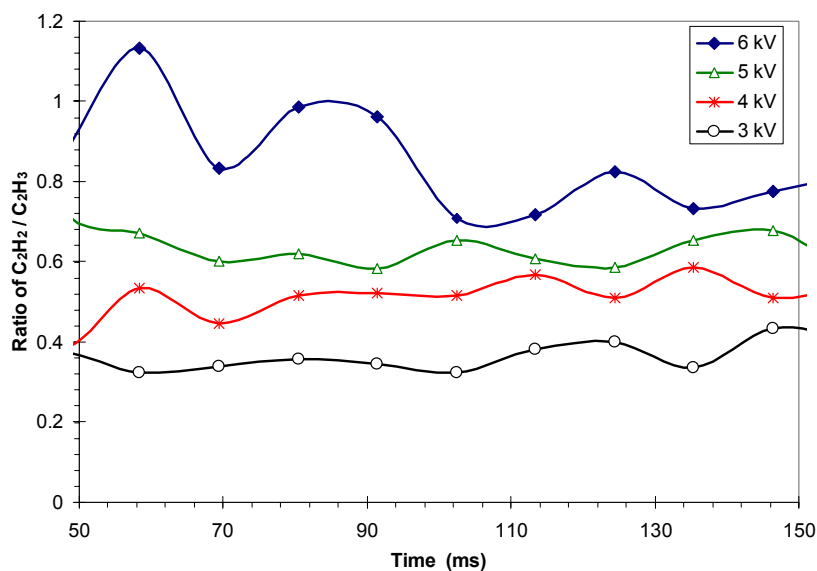

Figure 13. Effect of input energy on the ratio of species C_2H_2 over C_2H_3 (3.2 mm PE capillary).

Propellant species measurements were performed with a double-base propellant, JA2, and a composite propellant, M43. The propellant sample was placed about 13 mm downstream the secondary nozzle exit, and a 1.5mm hole provides a passage for any products from the propellant decomposition induced by the plasma interaction to reach the microprobe tip for sampling. The typical results are presented in Figure 14 and Figure 15 for JA2 and M43, respectively. In addition to the recombined species from the plasma, two other species coming from decomposition of the propellants were consistently detected for both propellants, which are NO and H_2CO, indicated by the mass 29 peak, which is a fragment of H_2CO formed during ionization.
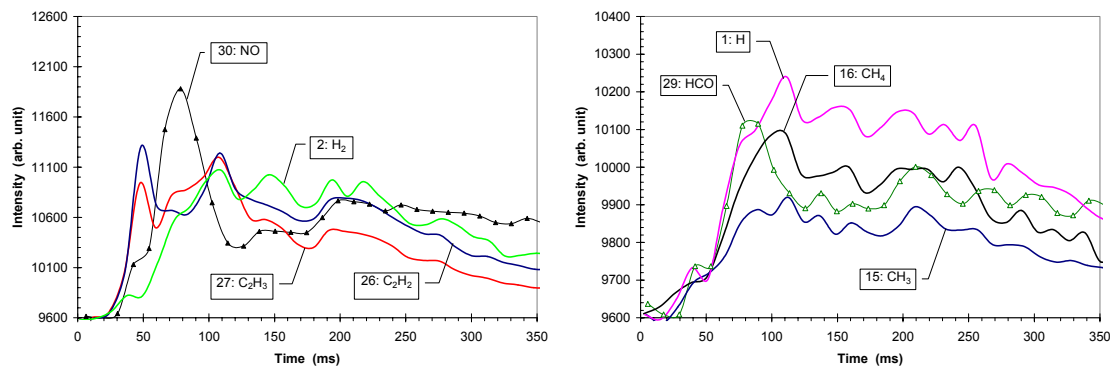
14

Figure 14. Species from plasma and decomposed JA2: major (left) and minor (right). Test conditions: 5kV, 3.2mm PE capillary, trigger plasma at 20ms.
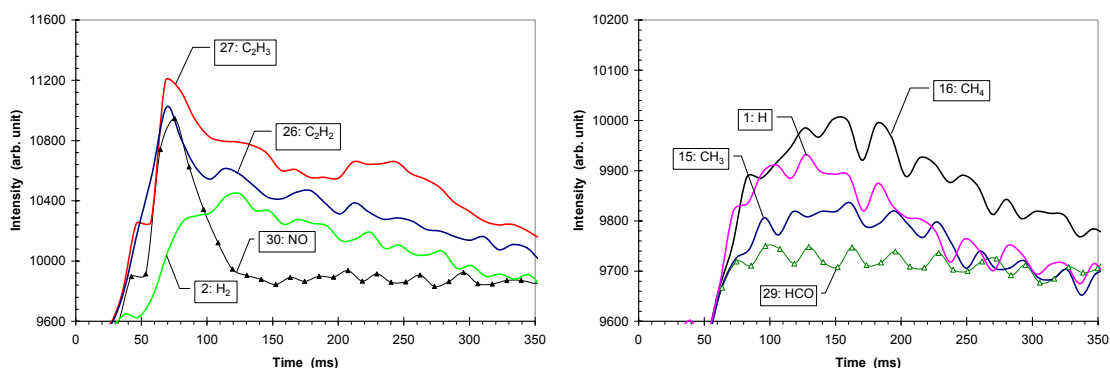

Figure 15. Species from plasma and decomposed M43: major (left) and minor (right). Test conditions: 6kV, 3.2mm PE capillary, trigger plasma at 20ms.
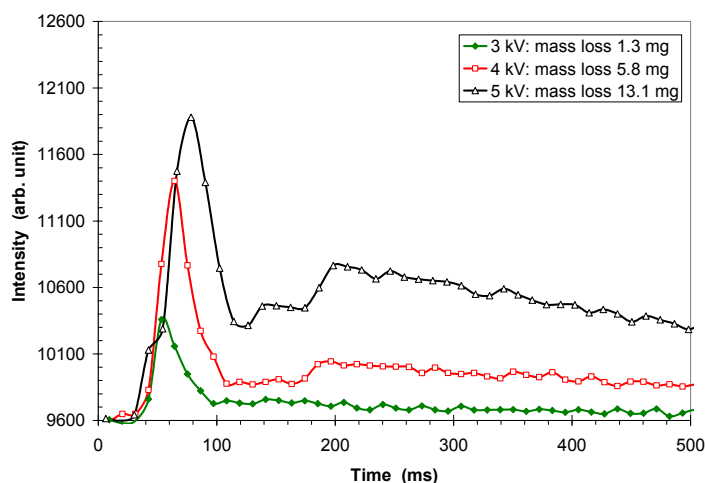

Figure 16. Effect of plasma energy on the yield of mass 30 (NO) from decomposition of JA2. Test conditions: 3.2mm PE capillary, trigger plasma at 20ms.

It is noted that NO is also seen in test with no propellant present, but in that case, its intensity is very small, likely coming from the interaction of plasma with the air in the holding chamber. Clearly, in tests with propellants, NO primarily comes from the propellants due to plasma-induced decomposition. On the basis of this, it is expected that the intensity of NO should increase as more propellant decomposes. This trend was verified by measurement of mass loss of the propellant after exposure to the plasma. Figure 16 shows the result that more propellant mass loss at higher plasma energy gives higher intensity of NO.

4.1.4 Radiative Heat Flux

An inverse data reduction technique was applied to the measured surface temperature to determine the absorbed, radiative heat flux. The numerical approach is described in detail in the text by Ozisik.[19] The model used a thermal conductivity $k = 0.25$W/m K, which is the normal conductivity obtained by Kurabayashi et al.,[23] $\rho = 1,420$ kg/m^3, and $c_p = 1,040$ J/kg K of the polyimide substrate. The temperature coefficient of the electrical resistivity of platinum $\beta = 0.002$/K was assumed to be linear over the temperature range from 20°C to 220°C, and it was deduced from measurements using a standard convection oven. This value is about 50% lower than the bulk value (0.00389/K). For the manufactured film thickness of 80 nm, the incident radiant energy is either absorbed or reflected by the platinum film; the transmissivity is practically zero. The theoretical spectral absorptivity of platinum can only be roughly estimated, since the film's properties appear to be quite far from representative of bulk values. Using bulk properties,[24] the diffuse or normal spectral absorptivity is about 0.75 at 200 nm, decreases to 0.4 at 400 nm, and about 0.32 at 600 nm. The platinum film appears slightly dark to the naked eye. A polyethylene capillary of 3.2 mm diameter was employed in all experiments.

Figures 17, 18, and 19 show the results from open-air testing involving a distance between plasma exit port to stagnation plate of 50 and 75 mm, as well as charging voltages of 2.5, 3.0 and 4 kV. Two Pearson current transducers were used to deduce the current and voltage in the plasma. Diode 1 (Si) is located directly below the plasma exit port, and is used to determine the time when the plasma emerges from the capillary into the ambient air environment. Diode 2 is also located below the plasma flow, but is placed about 48 mm from Diode 1. Both diodes thus have a side view of the plasma; their spectral range covers 300 to 900 nm. The diodes view the plasma through a 6 mm long, 0.71 mm diameter hole, and have a response time <10 ns. The incident power on the diodes is thus reduced significantly.
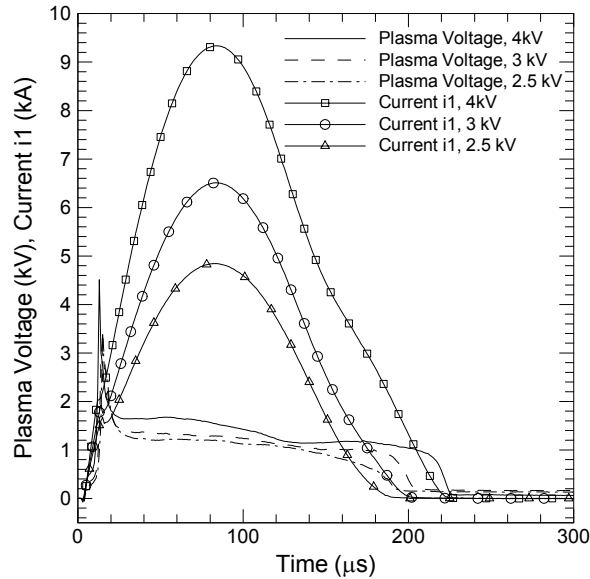

Figure 17. Current and voltage drop in electrical circuit with discharge in a 3.2 mm diameter polyethylene capillary for charging voltages of 2.5 (0.6kJ), 3kV (0.86kJ), and 4kV (1.56kJ).

Inspection of currents i1 in Fig. 17 reveals that peak values are reached at about 80 μs into the event, and they are fairly independent of charging level. However, the duration of electrical energy conversion varies from about 190 to 220 μs. Current i1 represents the current flow through the plasma chamber. At the end of the i1 current flow, there is still some residual energy in capacitor, however. It is slowly dissipated in the noninductive bypass resistor, which is used to deduce the instantaneous voltage drop across the plasma. The output from Diode 1, shown in Fig 18, reveals that the larger the charging voltage, the earlier the plasma emerges from the capillary into the ambient air. For example, a charging voltage of 4kV, it took 25 μs to emerge from the triggering event, whereas the corresponding time is 32

µs for a charging level of 2.5kV. Hence, times prior to plasma emergence are of little interest for both gas dynamic and heat transfer studies. The response of the second diode, shown in Fig. 19, does show the plasma emergence too at this early time, but this is caused by multiple reflections within the test facility. Diode 1, however, records a peak radiant heat fluxes that are much larger than Diode 2. The occurrence of the peak value of the heat flux of Diode 1 is close to the occurrence of the peak value of the current i1. Diode 2 detects reemission in some tests after the completion of the electrical discharge (t > 220 µs), which is probably due to interactions between plasma species and air as well as recombination reactions among the plasma products. For small charging levels, the emission from the plasma is quite small. Diode 2 senses emission only from regions near the stagnation plate; since it very low compared to Diode 1, the plasma has cooled significantly once reaching the stagnation plate. For low charging levels, emission occurs largely from copper and tungsten contained in the initiation wire and nozzle; emission from ablated capillary products is small.
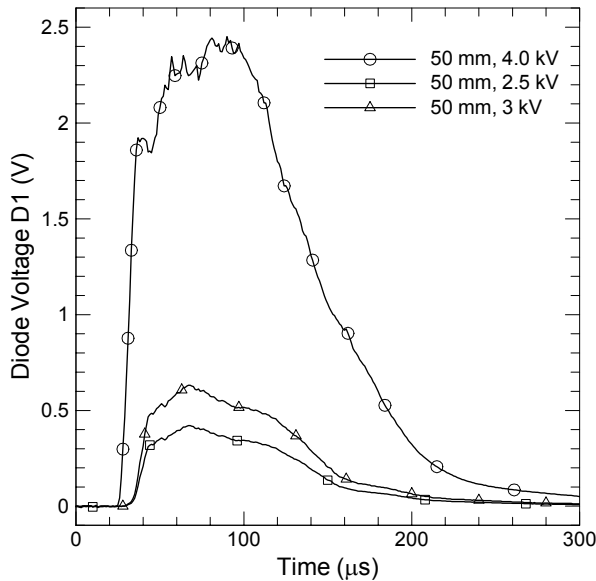

Figure 18. Response of Diode 1 due to emission from ablated products from polyethylene capillary, as well as initiation wire and nozzle for charging voltages of 2.5 (0.6kJ), 3kV (0.86kJ), and 4kV (1.56kJ).
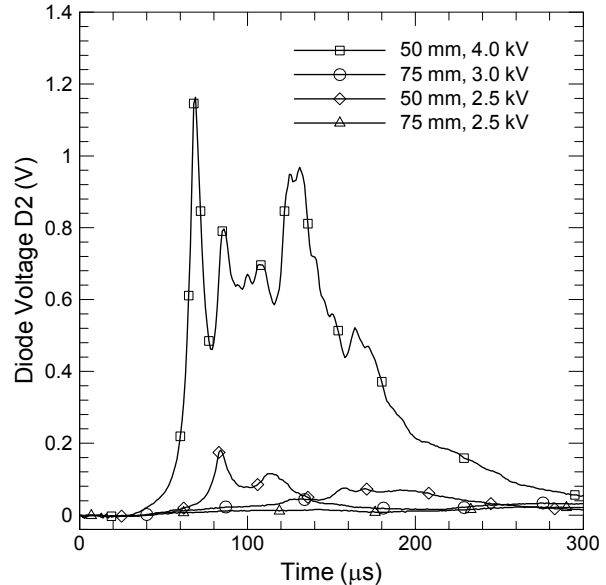
Figure 19. Response of Diode 2 due to emission from ablated products from polyethylene capillary, as well as initiation wire and nozzle for charging voltages of 2.5 (0.6kJ), 3kV (0.86kJ), and 4kV (1.56kJ).

The heat flux gauges were covered with two S1-UV fused silica windows from ESCO Products (one is 1/16" thick, whereas the other is 3/16" thick); this window material is very pure and allows transmission over the wavelength range from about 170 nm to 2,500 nm. The thin, sacrificial window is replaced after every test, since some slight degradation occurs of the surface. Additionally, only a small amount of sooty residue remains on the surface, in particular for the low charging level of 2.5kV. The LM134 constant current source is susceptible to interference from the rapidly changing electric and magnetic fields during the first 20 µs after triggering. Using a capacitor across the battery terminals has no effect. This interference is caused by two effects that produce high frequency electric and magnetic fields. First, as the initiation wire is rapidly heated to its melting point, its electrical conductivity rapidly decreases as the wire expands due to thermal effects and breaks apart to form small droplets. Second, as arching occurs between the droplets, a highly conductive metal vapor is rapidly produced that starts to ablate the wall of the capillary. As the vapor transitions from one containing metal ions and atoms to another containing carbon and hydrogen ions and atoms, as well as hydrocarbon ions and molecules, the

electrical conductivity changes again. Once the metal vapor has essentially been expelled into the nozzle, a quasi-steady voltage is achieved until the electrical energy is nearly discharged.

Figures 20 through 23 show the pressure, gauge temperatures, and deduced absorbed radiant heat fluxes for charging levels of 2.5 and 3kV and distances between plasma chamber and stagnation plate of 50 and 75mm; T_{ref}=20°C. The case shown in Fig. 20 yields the peak values: the film temperature rise is 160°C, the peak pressure is 8.8 bar, and the peak heat flux is 14.4 MW/m^2. Increasing the distance between plasma chamber and stagnation by 25 mm has a pronounced effect, as shown in Fig. 21. The peak film temperature is only 56°C and heat flux reaches a peak of only about 3.8 MW/m^2. Increasing the charging level from 2.5kV to 3kV, shown in Fig. 22, yields a doubling in the peak heat flux, whereas the electrical energy stored in the capacitor increased only by 44%. Examining the results for another gauge location, shown in Fig. 23, reveals a 20% reduction in the peak heat flux.   Hence the view factor between the plasma and gauge location is important, suggesting the need for multi-dimensional radiation models if this problem is to be studied using computational techniques. The gas dynamic phenomena revealed by the pressure gauges are complex as discussed previously, and captured in comprehensive modeling efforts by Nusca at ARL.[22]
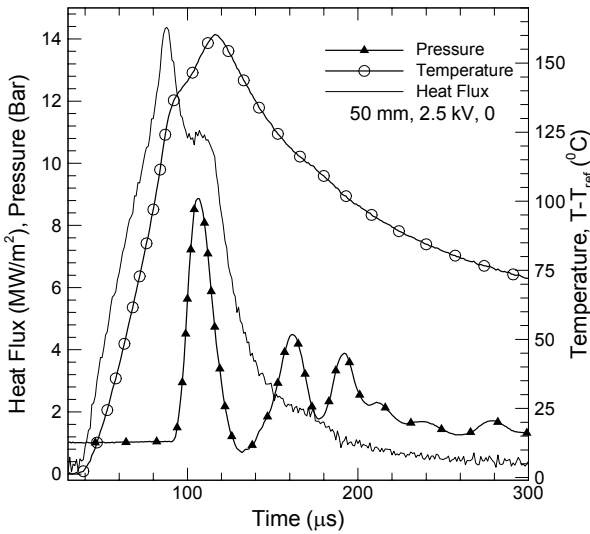

Figure 20. Pressure, temperature and heat flux at the stagnation location for a charging voltage of 2.5 (0.6kJ), and a distance of L = 50 mm between plasma port and stagnation plate.
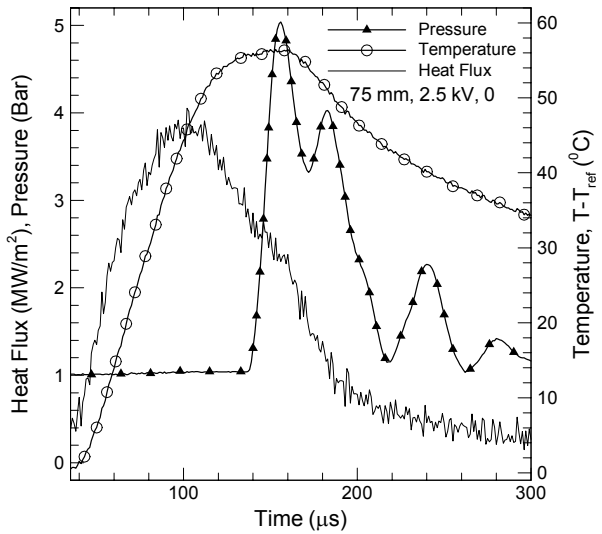
Figure 21. Pressure, temperature and heat flux at the stagnation location for a charging voltage of 2.5 (0.6kJ), and a distance of L = 75 mm between plasma port and stagnation plate.

The temperature rise is dominated by plasma emission during the time period prior to arrival of the precursor shock and thus shows a fairly smooth variation. The plasma quickly looses its sensible energy largely by radiation, and thus the gauge temperature decreases quickly due to primarily heat conduction into the substrate and secondarily to surface emission. Furthermore, inspection of Figs. 20 thru 23 reveals that the early portion of the plasma emission is the most intense, corresponding to the time period up to peak current flow, or peak power dissipation within the capillary. From other measurements, the plasma has traveled only about 40 mm at a time of 80 μs into the event.

Increasing the distance from 50 to 75 mm has a pronounced effect on all the peak values, demonstrating the important effect of gas dynamic expansion, directional nature of radiation, heat loss by radiation, and possibly recombination reactions among plasma species. A two-stage radiant heating effect is observed clearly in Figs. 20 and 23, whereas it only slightly detected in Fig. 21. The first stage is caused by the strong plasma emission prior to arrival of the precursor shock. The second stage is likely caused by increased pressure and temperature near the stagnation point, as plasma accumulates and

recombination reactions occur, some of which may produce emission due to electronic transitions in atomic and molecular species. Figures 20 and 23 show that small but measurable differences in pressure arrival and magnitude, as well as temperature and deduced radiant heat flux, occur between gauges located at the stagnation point and 9.5 mm above the stagnation point. The gas dynamic phenomena also show a slight phase shift in Figs. 20 and 23.
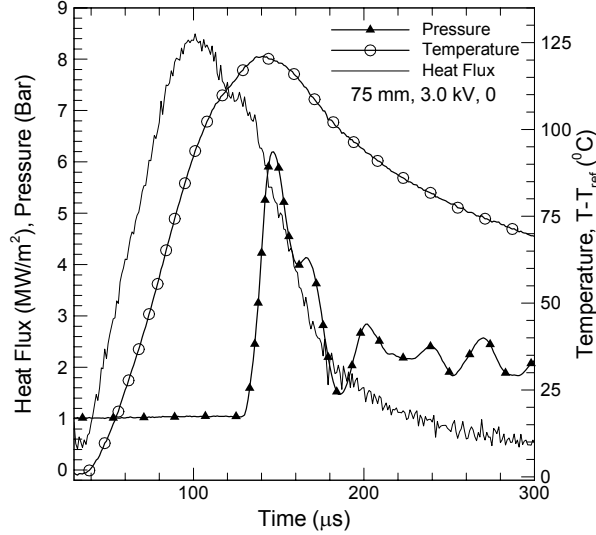

Figure 22. Pressure, temperature and heat flux at the stagnation location for a charging voltage of 3kV (0.86kJ), and a distance of L = 75 mm between plasma port and stagnation plate.
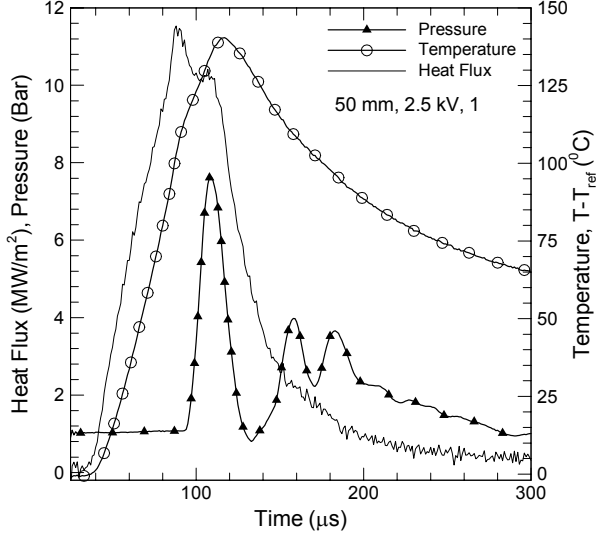
Figure 23. Pressure, temperature and heat flux 9.5 mm above the stagnation location (gauge 1) for charging voltage of 2.5 (0.6kJ), and a distance of L = 50 mm between plasma port and stagnation plate.

The plasma radiation is both spectral and directional, and has a nonlinear dependence on temperature. To push the gauges to their limits and beyond, we show in Figs. 24 and 25 the results for a charging level of 4kV and distance of 50 mm. Of the five gauges used on the stagnation plate, three were completely vaporized, a fourth was damaged, whereas the outermost gauge survived. Since the calibration was performed up to a temperature of 220°C, the results for gauges 0 and 2 are terminated near 280°C. The observed phenomena discussed previously are evident again, largely by gauge 4. Peak level of gauge 4 is slightly above 20 MW/m^2, whereas much higher values would be reached at the stagnation point. Plasma emission is dominant prior to arrival of precursor shock, some of the oscillating gas dynamic effects are present in the deduced radiative heat flux, and plasma emission is much lower after the electrical discharge is complete.

In order to assess the role of the fused silica window and its effect on the deduced radiative heat flux, Fig. 26 shows the results for gauges mounted 75 mm below the plasma port. These results were obtained from averaging data from three experiments and four heat flux gauges; the effect gauge position is not significant when mounting gauges below the plasma. Inspection of the results in Fig. 26 reveals that a reduction of only about 12 % is obtained by using the fused silica window. This reduction is quite acceptable, since the spectral transmissivity of the window ranges from about 0.92 at 200 nm to 0.94 at 700 nm (data from ESCO Products). Hence, the effect of the direction of the radiant energy emitted by the plasma on the deduced absorbed radiant flux levels in the previous figures is at best marginal. Furthermore, these results also suggest that the spectral range from about 200 nm to 2,500 nm of the fused silica window includes the dominant fraction of the radiant energy emitted by the plasma. Rovibrational transitions in the infrared wavelength range by molecular species, such C_xH_y, do not appear to contribute significantly to the radiative heat flux, although Diode 2 did record some effects from electronic transitions in the visible wavelength range well beyond the conclusion of the electrical power

conversion as mentioned previously. Additionally, the error bars included represent a 99% confidence interval, which is obtained by multiplying the standard deviation by 2.765.
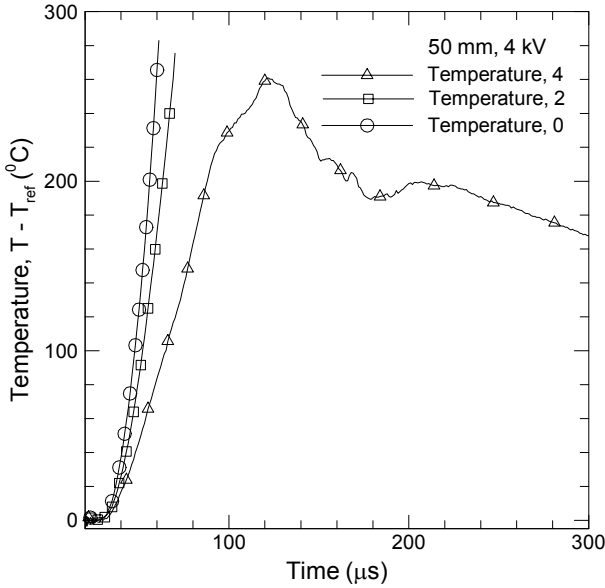

Figure 24. Temperature of three heat flux gauges separated by 19 mm on the stagnation plate, for a charging voltage of 4.0kV (1.56kJ), and a distance of L = 50 between plasma port and stagnation plate.
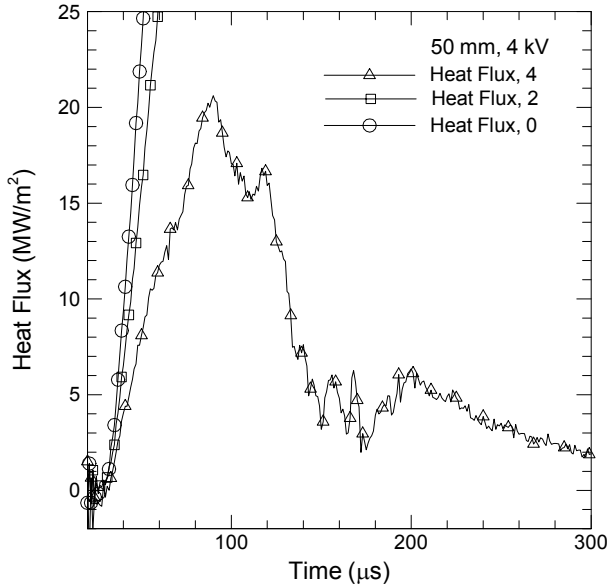

Figure 25. Deduced absorbed radiative heat flux of three gauges separated by 19 mm on the stagnation plate, for a charging voltage of 4.0kV (1.56kJ), and a distance of L = 50 between plasma port and stagnation plate
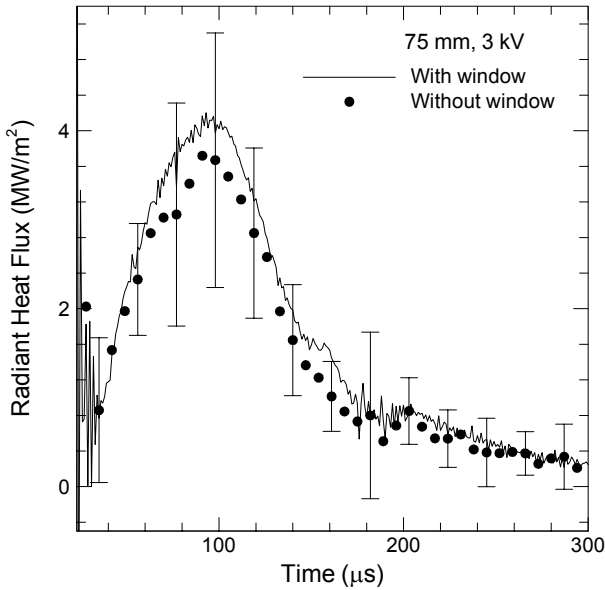

Figure 26. Effect of using the fused silica window on the deduced radiative heat flux for gauges located below the plasma.
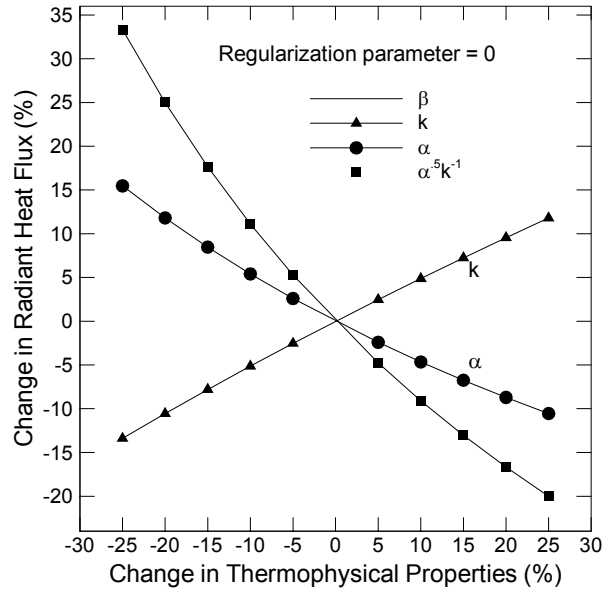

Figure 27. Effect of uncertainty in electrical and thermal transport data on the deduced radiative heat flux.

It is well known that inverse techniques are susceptible to error magnification. That is, a relatively small uncertainty in an input parameter may cause a large uncertainty in the estimated values. In the present combined experimental and numerical effort, the thermal conductivity of polyimide and the

temperature coefficient contain the largest uncertainty. Other input values are the product of density and specific heat, but the uncertainties of these values are usually much smaller. Figure 27 shows the effects of varying the input parameter on the estimated radiative heat flux. It observed that over the range of change in thermophysical properties, the response is reasonably linear.   Within the algorithm, the temperature coefficient β and the term $\alpha^{0.5}k^{-1}$ appear as a product, thus showing the identical results in Fig. 27. The uncertainty in the measured temperature coefficient is approximately 10%, suggesting a similar uncertainty in the estimated radiant heat flux. However, experiments will be conducted in the future to assess the thermal conductivity of the polyimide film, which may be anisotropic.

 To demonstrate the temporal effect of uncertainty in the input thermal conductivity and the temperature coefficient of the electrical resistivity, Figs. 28 and 29 show the results of the estimated radiative heat flux at the stagnation point for a distance of 50 mm between plasma port and stagnation plate, and a charging level of 2.5kV. These two input parameters were changed in increments with a maximum of $\pm$ 20% in the inverse technique. Inspection of these results show that the trends remain the same, and that peak values do not shift temporally. That is, a large uncertainty early in the event does not affect the results later in the event.
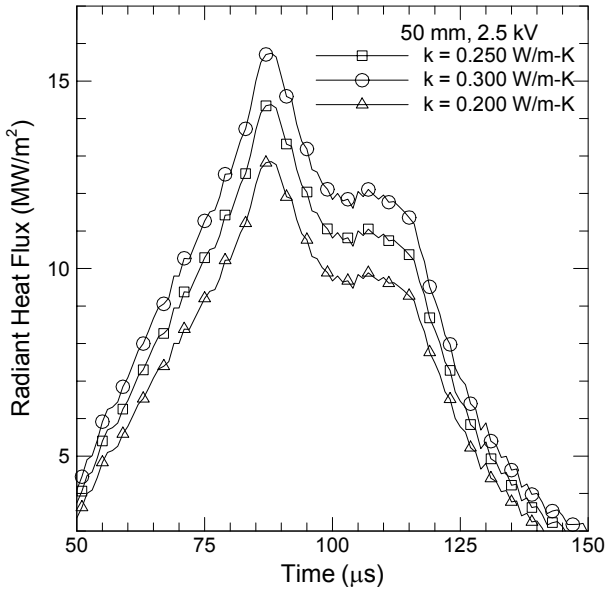
Figure 28.   Effect of uncertainty in thermal conductivity on the deduced radiative heat flux.
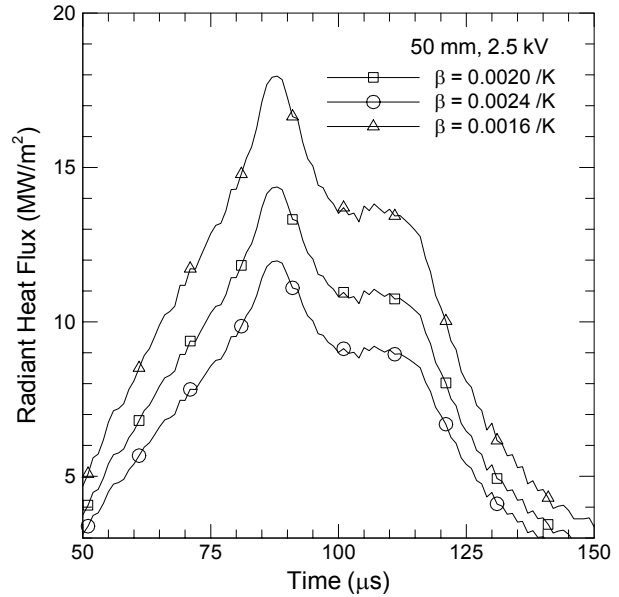
Figure 29.   Effect of uncertainty in the temperature coefficient of the electrical resistivity on the deduced radiative heat flux.

4.2   Plasma-Propellants Interaction

4.2.1   Open Air Testing

 The open-air impingement tests were conducted with a fixed nozzle-to-plate distance, but a varied nozzle-to-sample distance (L_{n-s}) by adjusting a threaded sample holder. Three gun propellants were used in these tests, a double-base propellant, JA2, and two nitramine composites, M43 and XM39. JA2 is somewhat translucent; whereas M43 and XM39 are completely opaque. At ambient conditions, JA2 is much more flexible compared to the other two, and M43 is the most brittle one among the three. All these propellants are cylindrical sticks having a diameter of 10.9 mm. JA2 has seven perforations, each having a diameter about 0.5 mm. M43 and XM39 have no perforation.

 Thin disks were cut from sticks for testing. In the microscopy study, all disk samples have a typical thickness around 1.5 mm, and samples of M43 and XM39 were polished prior to plasma exposure since cutting from sticks results in a very rough surface. With a thickness of 1.5 mm, samples were sometimes

broken into several pieces upon the impingement of plasma when sample-to-nozzle distances were small; this was especially true for M43 and XM39. As a result, a relatively large spacing (L_{n-s} = 25 mm) was used in tests designed for microscopic observation. To avoid fracture during open-air tests for measuring ablation masses, thicker samples of about 4 mm were used. However, even with this thickness, samples of M43 and XM39 (especially M43) tended to fragment into several pieces at higher discharge energy and/or closer nozzle-to-sample distances. To be sure that all sample pieces were recovered, a relatively large enclosure of aluminum foil was used, and an averaged mass loss from three tests was determined.

In the open-air testing, parametric studies were performed with variations of L_{n-s} ranging from 3 mm to 25 mm and of charging voltage from 2 to 6 kV corresponding to energy levels ranging from 0.38 kJ to 3.46 kJ. Regardless of the conditions, ignition did not occur; the failure to achieve ignition was most likely due to the lack of confinement, since ignition threshold has been shown to be a strong function of confinement. However, the open-air configuration provides an easier way to determine propellant mass losses prior to ignition due to ablation by plasma, since it avoids the need to interrupt the test by, for example, reducing the chamber pressure.

Figure 30(a) presents typical results for mass losses of the three propellants subjected to head-on normal impingement of the plasma at different nozzle-to-sample distances. These tests were conducted using a charging voltage of 4 kV (E = 1.56 kJ). Another series of tests were performed at a fixed value of L_{n-s} but at four different energy levels. These results are presented in Fig. 30(b). Table 1 lists the mass losses due to ablation for each individual test, and the information about fragmentation is also included. As can be seen from both sets of results, under the same test conditions, JA2 often has the largest amount of mass loss. Also, the data show the expected trends that higher discharge energy and smaller L_{n-s} both result in increasing mass loss. Another interesting observation is that at higher discharge energy or smaller L_{n-s} values, all three propellants tended to fragment into a few (sometimes many) small pieces (see Table 1 for fragmentation information). This fragmentation would be expected to augment the burn rate.
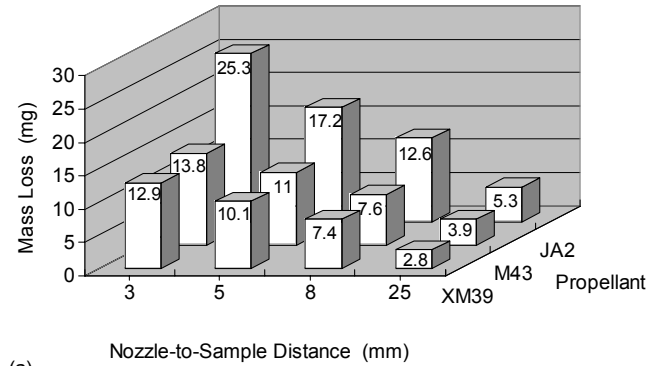
(a)
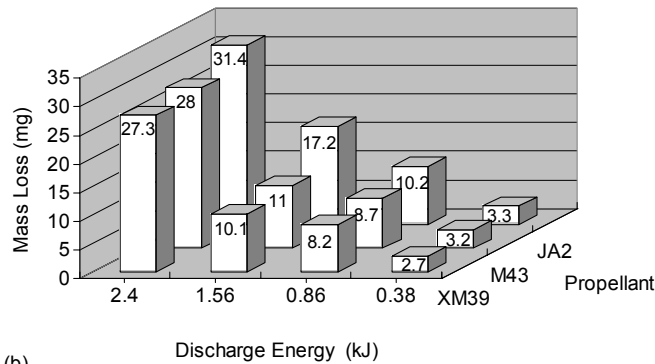
(b)

Figure 30. Ablation masses of the propellants: (a) E = 1.56 kJ; (b) L_{n-s} = 5 mm.

Two processes can contribute to the mass loss during exposure to the plasma: surface ablation and in-depth eruptive ejection. Surface ablation is caused by intense heating that melts and vaporizes the surface material. During the ablation process, a thin layer of vapor will develop between the plasma and the propellant surface to form a vapor shield, which causes a reduction in the radiative energy transport to the propellant surface, suggesting that the plasma kinetic energy may be more important than radiative heat flux. It should be noted that, for the perforated JA2, its seven perforations provide more exposed surface area than the non-perforated composite propellants. However, examination of recovered JA2 samples indicates only a slight enlargement of the perforation (about 0.03-0.05 mm in diameter and 1-1.5 mm in depth), which occurred when higher energy and smaller L_{n-s} were used, and thus, the ablation mass from the perforations accounts for a small portion (about 5%) of the total amount. Eruptive ejection is a result of the formation of high-pressure gas bubbles in sub-surface regions due to in-depth radiative heating, which can occur depending on the optical properties of the propellants.

Table 1: Test-to-test variation in ablation masses of propellants in open-air testing

Test condition		m_{ab_JA2}, mg				m_{ab_M43}, mg				m_{ab_XM39}, mg			
E, kJ	L_{n-s}, mm	Test1	Test2	Test3	aver.	Test1	Test2	Test3	aver.	Test1	Test2	Test3	aver.
0.38	5	3.2	3.3	n/a	**3.3**	3.0	3.3	n/a	**3.2**	2.6	2.8	n/a	**2.7**
0.86	5	9.8	10.5	n/a	**10.2**	8.2	9.1	n/a	**8.7**	7.9	8.5	n/a	**8.2**
1.56	5	16.4	17.2	18.0	**17.2**	9.8[a]	11.4[a]	11.9	**11.0**	9.2	10.1[a]	11.0	**10.1**
2.40	5	29.9[a]	31.5	32.7	**31.4**	27.2[b]	27.8[b]	29.0[b]	**28.0**	26.0[b]	27.4[b]	28.4[b]	**27.3**
1.56	3	24.6	25.3	26.0[a]	**25.3**	12.6[b]	14.0[a]	14.8[a]	**13.8**	12.3[a]	12.9[a]	13.6	**12.9**
1.56	8	12.2	12.6	12.9	**12.6**	7.1	7.7[a]	8.0	**7.6**	7.3	7.4	7.6	**7.4**
1.56	25	5.1	5.4	n/a	**5.3**	3.8	4	n/a	**3.9**	2.7	2.8	n/a	**2.8**

[a] tests with propellant fragmentation (2-5 pieces)
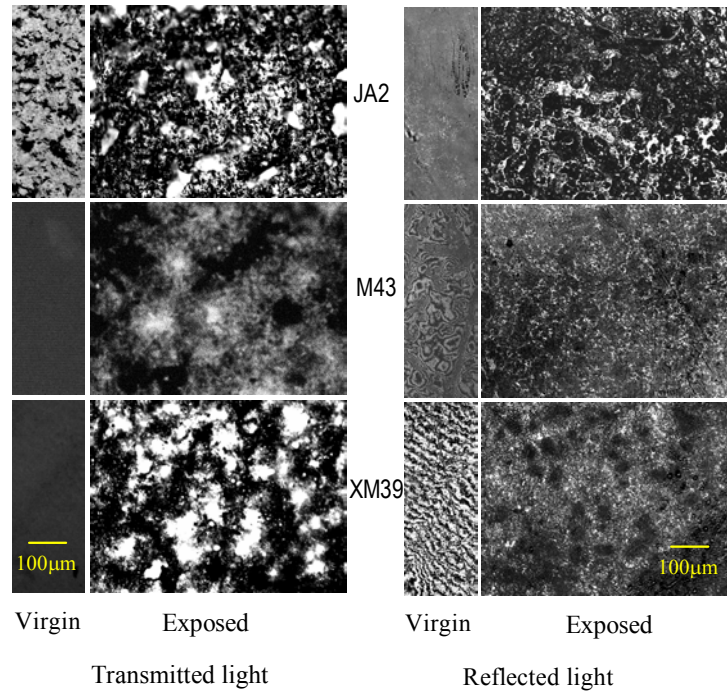[b] tests with propellant fragmentation (more than 5 pieces)

Figure 31. Microscopic images of plasma-exposed propellant samples (E = 3.46 kJ, L_{n-s} = 25 mm).

Propellant samples recovered after the tests show significant changes in color and surface structure. Optical microscopic photos of typical results are shown in Fig. 31, where both confocal LSM (reflected light) and DIC (transmitted light) images are presented. Images of virgin samples are included for comparison. Surface modification and/or in-depth structural change were observed for all samples.

Tests of JA2 with higher discharge energies and shorter L_{n-s} values usually resulted in color change from dark-green to yellow-green in a layer from the exposed surface down to about 1 to 1.5 mm of the sample, and internal voids and blisters were observed along the side surface of this layer. A very roughly pitted area about 6 mm in diameter that was recessed about 0.5-1.0 mm from the original surface was found in the region that was directly exposed to the plasma. Also, deformation of the affected layer causes slight enlargement of the diameter. Figure 32 shows two JA2 samples recovered after being exposed to plasma (5 kV charging voltage with L_{n-s} = 5 mm); one of the samples fragmented due to its small thickness (Fig. 32b).
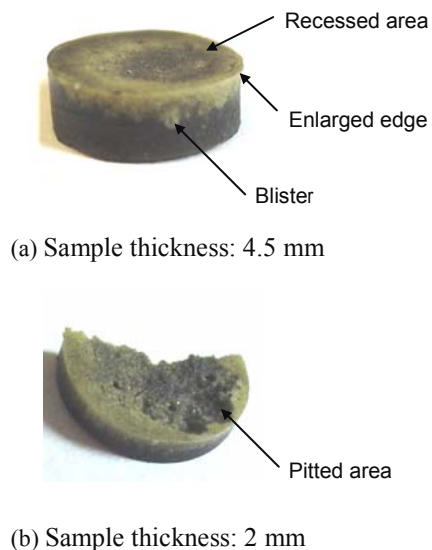

(a) Sample thickness: 4.5 mm

(b) Sample thickness: 2 mm

Figure 32. Photos of recovered JA2 samples (E = 2.40 kJ, L_{n-s} = 5 mm).

These observations are strong indicators that in-depth heating causes decomposition of the propellant. Some of the gaseous decomposition products accumulated in bubbles that burst, leaving pits in the surface; others remained trapped inside the propellant resulting in internal bubbles and/or blisters. Chemical analysis of NO levels in recovered JA2 samples by Beyer *et al.*[25] and Pesce-Rodriguez *et al.*[26] using desorption-gas chromatography-mass spectroscopy (D-GC-MS) indicated enhancement of NO formation down to a depth of 0.75 mm from surface, and suggested that NO is an early product of decomposition of nitrate esters and is sufficiently stable to remain trapped inside the sample. The color of the strongly affected region looks black as a result of some residual deposits from the plasma; Taylor[27] suggested that the black region results from deposition of copper oxide (CuO). Slight enlargement ranging from 0.03 to 0.05 mm in the perforations was observed on the exposed side of the JA2 sample, and the affected depth is about 1-1.5 mm, corresponding to a mass loss about 1-2 mg.

The responses of M43 and XM39 were similar to each other but quite different from that of JA2. The surfaces of M43 and XM39 were blackened, but otherwise no color change was observed. Pits were found in the affected surface areas for these materials, but no blisters or recessed areas were formed. These results suggest that radiative and conductive heating is restricted to a very thin layer in the near-surface zone, and mass losses are caused by surface ablation only. The lack of in-depth effects of the plasma is consistent with the fact that these propellants are opaque, whereas JA2 is somewhat translucent*;* this effect agrees with the findings by Koleczko *et al.*[28] The differences between the JA2 and the

composite propellants are expected to affect their behavior during ignition and combustion, as will be seen in the closed-chamber results presented in next section.

4.2.2   Closed Chamber Testing

Closed-chamber testing was conducted in the configuration similar to that shown in Fig. 2 to study the plasma ignition and combustion behavior of the three propellants. For each test, approximately 500 mg of propellant was used, corresponding to a loading density about 0.08 g/cm^3. The plasma impinged normally to the sample surface at a nozzle-to-sample distance of 5 mm, which is a very aggressive condition for mass loss, ignition and burn rate enhancement.[29] The capacitors were charged to 5 kV (E = 2.40 kJ), with about 2.36 kJ energy deposited into the plasma.
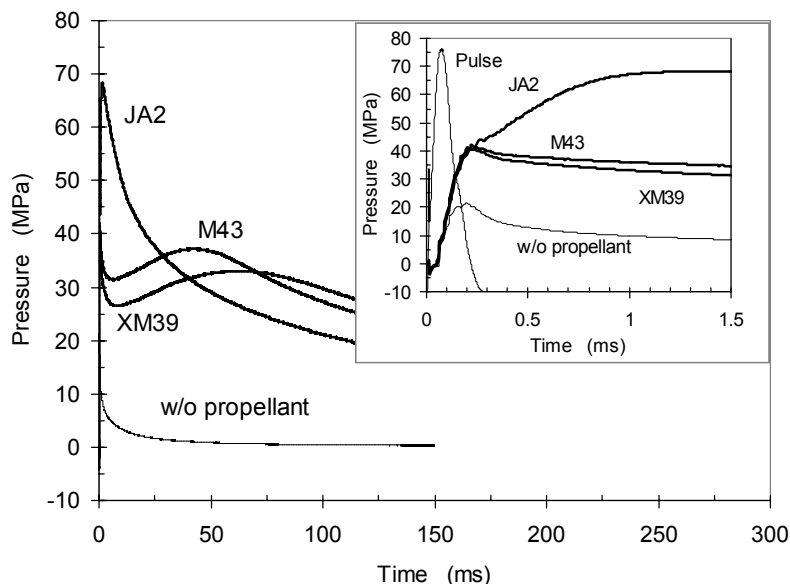

Figure 33. Comparison of ignition and burning for JA2, M43 and XM39 (E = 2.40 kJ).

Pressure histories were recorded for these tests as well as the baseline case with no propellant. Typical results are plotted in Fig. 33 on two time scales, 0 to 300 ms and 0 to 1.5 ms. The shorter time scale plot includes the plasma power to indicate the duration of the plasma pulse. The results show significant differences in both ignition delay and overall burn rate of JA2 and the composite propellants, XM39 and M43. The pressure traces of the composite propellants indicate a two-stage burning behavior, which is most clearly visible for the composite propellants in Fig. 33. During the first stage, which occurs within the plasma pulse, chamber pressure rises rapidly above the pressure caused by the plasma alone (curve labeled "w/o propellant" in Fig. 33.) The increased pressure is caused by the ablation and/or combustion of the propellant. This rapid rise is followed by a decrease in pressure, indicating that the propellant has not ignited. After a delay, the pressure begins to rise again, indicating that the propellant has ignited due to exposure to the high temperature gases in the chamber; during the second stage, the propellant burns to completion.

Table 2 presents several events of interest during ignition and combustion. The times presented correspond to peak power ($\tau_{\text{peak-power}}$), first peak pressure ($\tau_{\text{peak-pressure}}$), end of pulse ($\tau_{\text{end-of-pulse}}$), start of second stage ($\tau_{\text{second-stage}}$), and completion of combustion ($\tau_{\text{end-of-combustion}}$). These particular times are also illustrated in Fig. 34. The events that are characteristic of plasma-driven ignition and combustion are quite similar for the three propellants. In fact, within the duration of the plasma pulse (or the first stage of burning), the responses of all three propellants, including the pressure rise, are surprisingly similar. A clear delay period after the plasma-driven burning is present only for the composite propellants. Burning

25

in the second stage is much slower as indicated by the large values of $\Delta\tau$ listed in Table 2. XM39 exhibits a longer second stage than M43.

Table 2 Summary of plasma-ignition and combustion of JA2, M43 and XM39 (E = 2.40 kJ)

Propellant type	$\tau_{\text{peak-power}}$, ms	$\tau_{\text{peak-pressure}}$, ms	$\tau_{\text{end-of-pulse}}$, ms	$\tau_{\text{second-stage}}$, ms	$\tau_{\text{end-of-combustion}}$, ms	$\Delta\tau$,[a] ms
JA2	0.081	0.230	0.310	0.31	1.38	1.07
M43	0.078	0.240	0.300	3.24	42.25	39.01
XM39	0.078	0.245	0.310	3.70	62.50	58.80

[a] $\Delta\tau = \tau_{\text{end-of-combustion}} - \tau_{\text{second-stage}}$

During the first stage, the pressure rise is a combining result of the plasma expansion and ignition and burning of part of the propellant, which includes the ablated mass and part of the main charge. This portion of the propellant is ignited and burned to final products at a very high burn rate as a result of the plasma enhancement. The plasma-enhanced burning within the pulse (the first stage) appears to be quite similar among the propellants.
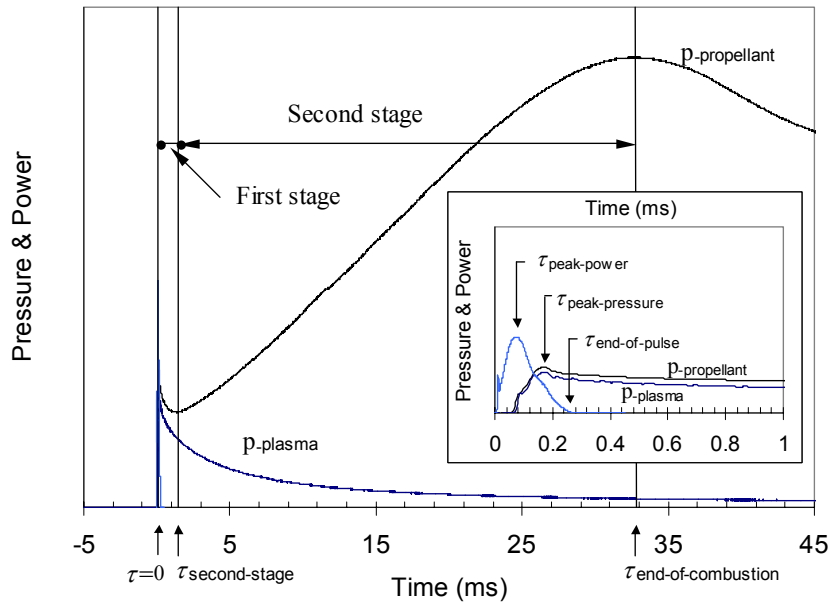

Figure 34. Illustration of two-stage burning behavior of ETC plasma-ignited propellants.

To estimate the amount of propellant mass that is consumed in the first stage in the closed chamber tests, an energy balance was performed based on the increase in chamber pressure caused by the burning of the propellant.   Subtracting the pressure without propellant from the pressure with propellant yields the pressure data required for the analysis; the pressure difference curves resulting from this subtraction are plotted in Fig. 35. For the energy balance, the chamber volume is the control volume, and the combustion products are modeled as a mass generation source. Applying the First Law of Thermodynamics to the control volume and neglecting heat transfer to the walls give an apparent mass generation rate that is related to the pressure variation, i.e.,

$$\dot{m} = \frac{c_v V}{c_p R T_g / MW} \frac{dp}{dt}$$

where *MW* is the molecular weight of the combustion products and *V* is the chamber volume. The mass loss at any time of interest can be calculated by integration of above equation.   Neglecting the heat losses to chamber walls is not expected to introduce a large error given the short time over which the calculation

is performed. Also, the subtraction scheme will minimize the error caused by neglecting the effect of heat loss since it should reduce the effects of heat loss from the plasma gases.
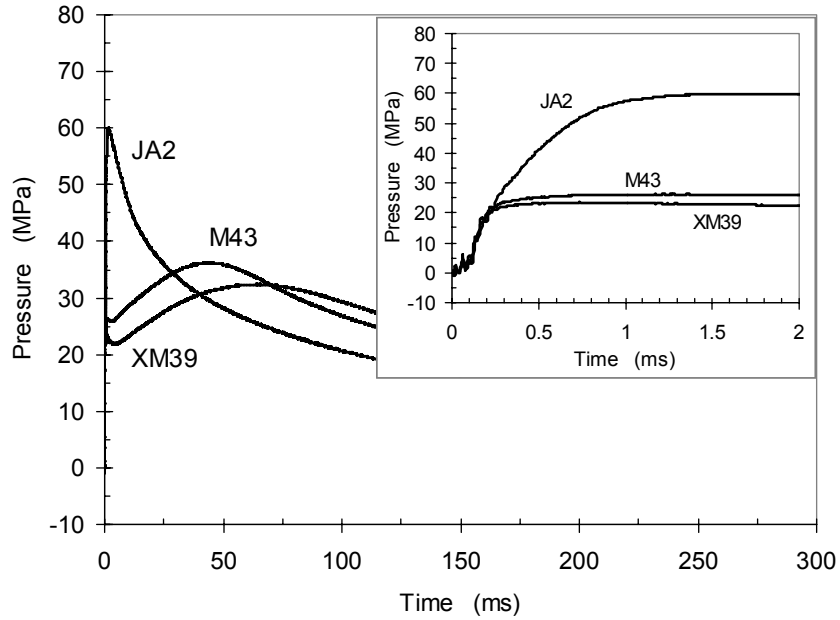

Figure 35. Comparison of pressure increase as a result of combustion of the propellants.

The total propellant mass calculated through the energy balance is less than the mass of propellant used in the tests. Consequently, the gasification rate is scaled so that the total mass from the calculation matches the propellant mass used. Table 3 summarizes the calculated mass loss at several particular time intervals that are listed in Table 3, i.e., $m_{peak-power}$, $m_{peak-pressure}$, and $m_{end-of-pulse}$ correspond to $\tau_{peak-power}$, $\tau_{peak-pressure}$, and $\tau_{end-of-pulse}$, respectively. For comparison, the measured plasma-induced mass losses ($m_{measured}$) from open-air experiments are included as well. These results are also presented in Fig. 36.

Table 3 Calculated gasification of JA2, M43 and XM39 within the plasma pulse

Propellant type	$m_{peak-power}$, mg	$m_{peak-pressure}$, mg	$m_{end-of-pulse}$, mg	$m_{measured}$, mg
JA2	17.9	147.4	196.9	31.7
M43	16.6	248.4	290.0	28.0
XM39	18.2	258.5	286.9	27.3

Based on the calculation, the total mass conversion from solid to gas within the plasma pulse ($m_{end-of-pulse}$) is much greater than the mass loss measured in open-air testing, $m_{measured}$. It is not unreasonable for the closed-chamber tests to give higher values since higher gas densities will occur within the subsonic regions near the sample surface, and the higher densities should enhance heat transfer to the sample, resulting in increased mass conversion rates from solid to gaseous products. Moreover, it is likely that $m_{end-of-pulse}$ involves not only the mass loss due to ablation but also due to combustion of propellant that occurs during the first-stag; the latter represents a major fraction of $m_{end-of-pulse}$. It should be noted that the value of $m_{end-of-pulse}$ for JA2 is smaller than that for the two composites, which is opposite of the trend for the open-air ablation mass, $m_{measured}$, in which JA2 has a larger value than the composites. This opposite trend suggests that, in the closed-chamber testing, the composites have more mass burned during the plasma pulse. During open air testing the composite propellants fragmented into more pieces than JA2,

which often did not fragment at all. Thus, fragmentation of the composite samples may account for their faster combustion during the plasma pulse.
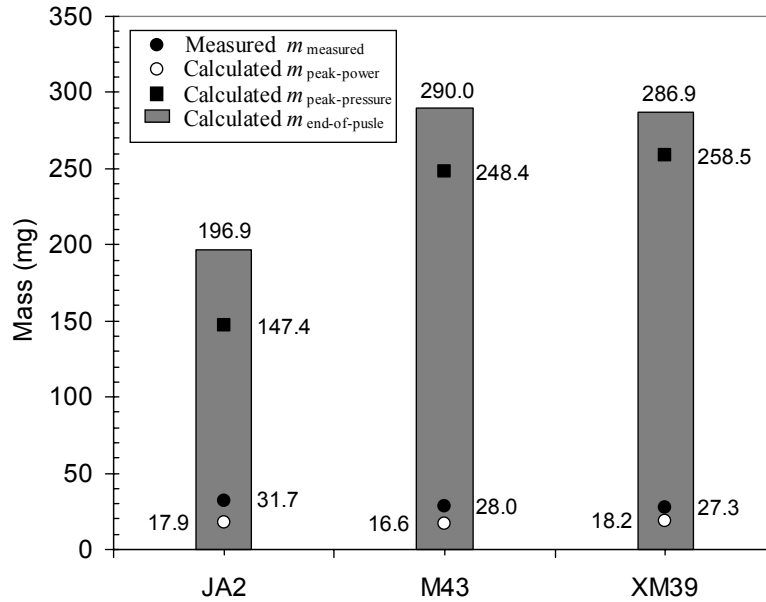

Figure 36. Comparison of measured ablation mass with calculated values (E =2.40 kJ).

The calculated gas generation rates for the three propellants are presented in Fig. 37, which also includes the combustion pressure curves and the plasma power to indicate the pulse width. The energy balance requires the time derivative of the pressure, which is affected by noise that causes significant scatter in the gas generation rates. To minimize this effect, a 500Hz low-pass filter was used to remove high-frequency components in the original data. Multiple peaks in gasification rates are present for all propellants, which may correspond to gasification of the ablated mass, combustion of the ablated mass, and combustion of part of the main propellant charge. The gas generation rate curves during the plasma pulse look similar for the three propellants, but JA2 has a lower peak value.
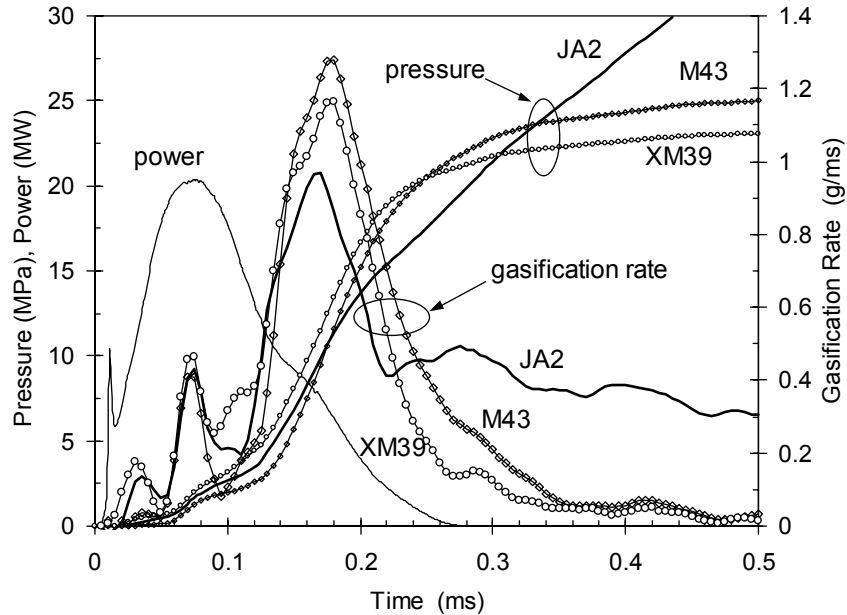

Figure 37. Comparison of gas generation rates in early stage of burning.

5 PUBLICATIONS AND REPORTS

5.1 Papers Published in Peer-reviewed Journals

Li, J.-Q., Litzinger T., A., and Thynell, S., T., "Interactions of Capillary Plasma with Double-base and Composite Propellants," accepted for publication in *Journal of Propulsion and Power*, to appear May-June, 2004.

Li, J.-Q., Litzinger, T., A., and Thynell, S., T., "Plasma Ignition and Combustion of JA2 Propellant," accepted for publication in *Journal of Propulsion and Power*, April, 2004.

5.2 Papers Published in Non-peer-reviewed Journals or in Conference Proceedings

Li, J.-Q., Litzinger, T. A., and Thynell, S. T., "Experimental Investigation of Plasma-Ignition and Combustion of Solid Propellants," *Proceedings of the 39th JANNAF Combustion Subcommittee Meeting*, Colorado Springs, Colorado, December 1-5, 2003.

Li, J.-Q., H. Zhou, G. Kudva, T. A. Litzinger and S. T. Thynell, "Experimental Investigations of Plasma Propellant Interactions," Proceedings of the 37th JANNAF Combustion Subcommittee Meeting, Vol. 37, March, 2001.

5.3 Papers Presented at Meetings, but not Published in Conference Proceedings

J.-Q. Li, J.H. Kwon, H. Zhou, G. Kudva, S. T. Thynell and T. A. Litzinger, "Experimental Investigations of Characteristics of Electro-Thermal-Chemical Plasma," AIAA paper, 2001-3855, 37th AIAA/ASME/SAE/ASEE Joint propulsion Conference and Exhibit, July 8-11, 2001, Salt Lake City, Utah.

5.4 Manuscripts Submitted, but not Published

Das, M., S. T. Thynell, J.Q. Li, and T. A. Litzinger, "Transient Radiative Heat Transfer from an Electro-thermal-chemical Plasma," in preparation for submission to *AIAA journal of Propulsion and Power*.

5.5 Technical Reports Submitted to ARO
None

6 PARTICIPATING SCIENTIFIC PERSONNEL
Professor Stefan T. Thynell
Professor Thomas A. Litzinger
Mr. Jianquan Li, Ph.D. candidate (defended thesis on April 13, 2004)
Mr. Malay Das, Ph.D. candidate (passed candidacy exams)
Mr. Sameet Nabar, Ph.D. candidate (passed PhD candidacy exams)

Mr. Vikrant Saxena, Ph.D. student

Mr. Hasan Rouf, Ph.D. student

Mr. Hualiang Zhou, M.S. degree conferred December, 2000

Mr. Jae Kwon, M.S. degree August 15, 2004

Mr. K. Miller, Undergraduate Student

7 REPORT OF INVENTIONS
None

8 TECHNOLOGY TRANSFER
Significant interaction occurred with technical staff at the Army Research laboratory, including among others Dr. Kevin White, Mr. Tony Williams, Dr. Mike Nusca, Dr. Dick Beyer, and Dr. Rose Pesce-

Rodriguez. We appreciate the receipt of ignitrons, capacitors, inductor, and current transducer. Drs. Thynell and Litzinger have made yearly presentations of progress at ARL, and participated in several workshops. We maitain contact with Dr. Michael Nusca, who continues to model one of the experimental configurations for studying the plasma/propellant interaction. We also appreciate the design drawings of the plasma chamber, obtained from the UT Austin group. Finally, we are also grateful to Dr. Johnny Yu at ATK-Radford Army Ammunition Plant for shipment of the JA2 propellant.

9 REFERENCES

[1] Katulka, G. L., and Dyvik, J., "Experimental Results of Electrical Plasma Ignition in 120-mm Solid Propellant Tank Gun Firings," Proceedings of the 33rd JANNAF Combustion Subcommittee Meeting, CPIA Publication 653, Vol. III, pp. 103-110, November 1996.

[2] Marinos, C., "ETC Ignition and Temperature Sensitivity," Proceedings of the 32nd JANNAF Combustion Subcommittee Meeting, CPIA Publication 631, Vol. III, pp. 109-118, October 1995.

[3] Dyvik, J. A., and Katulka, G., "ETC Temperature Compensation: Experimental Results of 120-mm Test Firings," Proceedings of the 33rd JANNAF Combustion Subcommittee Meeting, CPIA Publication 653, Vol. II, pp. 111-119, November 1996.

[4] Perelmutter, L., Sudai, M., Goldenberg, C., Kimhe, D., Zeevi, Z., Arie, S., Melnik, M., and Melnik, D., "Temperature Compensation by Controlled Ignition Power in SPETC Guns," Proceedings of the 16th International Symposium on Ballistics, pp. 145-152, September 1996.

[5] Del Guercio, M., "Propellant Bun Rate Modification by Plasma Injection," Proceedings of the 34th JANNAF Combustion Subcommittee Meeting, CPIA Publication 662, Vol. I, pp. 35-42, October 1997.

[6] White, K. J., Katulka, G. L., Khuan, T., and Nekula, K., "Plasma Characterization for Electrothermal-Chemical (ETC) Gun Applications," ARL-TR-1491, Army Research Laboratory, Aberdeen Proving Ground, MD, September 1997.

[7] Nusca, M. J., and White, K. J., "Plasma Radiative and Convective Interactions with Propellant Beds," Proceedings of the 34th JANNAF Combustion Subcommittee Meeting, West Palm Beach, FL, October 1997.

[8] Kohel, J. M., Su, L. K., Clemens, N. T., Varghese, P. L., and Raja, L., "Experimental Characterization of a Pulsed Plasma Jet," AIAA 98-0999, 36th Aerospace Sciences Meeting and Exhibit, Reno, NV, 1998.

[9] Kohel, J., Su, L. K., Clemens, N. T., and Varghese, P. L., "Emission Spectroscopic Measurements and Analysis of a Pulsed Plasma Jet," *IEEE Transactions on Magnetics*, Vol. 35, pp. 201-206, 1999.

[10] Kim, J. U., Clemens, N. T., and Varghese, P. L., "Experimental Study of an Underexpanded Pulsed Plasma Jet," AIAA 99-0452, 37th Aerospace Sciences Meeting, Reno, NV, 1999.

[11] Raja, L. L., Varghese, P. L., and Wilson, D. E., "Modeling of the Electrogun Metal Vapor Plasma Discharge," *AIAA Journal of Thermophysics and Heat Transfer*, Vol. 11, pp. 353-360, 1997.

[12] Nusca, M. J., White, K. J., Williams, A. W., Landsberg, A. M., Young, T. R., and Lind, C. A., "Computational and Experimental Investigations of Open-Air Plasma Discharges," AIAA 99-0865, 37th Aerospace Sciences Meeting and Exhibit, Reno, NV, 1999.

[13] Li, J. Q., Kwon, J., Thynell, S. T., and Litzinger, T. A, "Experimental Investigations of Characteristics of Electro-Thermal-Chemical Plasma," AIAA paper 2001-3855, presented at the Joint Propulsion Conference, Salt Lake City, Utah, July 8-11, 2001.

[14] Lee, Y. J., Tang, C. J., Kudva, G., and Litzinger, T. A., "A Triple Quadrupole Mass Spectrometer System for Studies of Gas-phase Chemistry of Energetic Materials," *Measurement Science and Technology,* Vol. 9, pp. 1576-1586, 1998.

[15] Piccini, E., Guo, S. M., and Jones, T. V., "The Development of a New Direct-Heat-Flux Gage for Heat-Transfer Facilities," Measurement Science and Technology, Vol. 11, pp. 342-349, 2000.

[16] Anthony, R. J., Oldfield, M. L. G., Jones, T. V., and LaGraff, J. E., "Development of High-Density Arrays of Thin Film Heat Transfer Gages," Proceedings of the 5th ASME/JSME Thermal Engineering Joint Conference, San Diego, CA, March 1999

[17] Walker, D. G. and Scott, E. P., "Evaluation of Estimation Methods for High Unsteady Heat Fluxes from Surface Measurements," *AIAA Journal of Thermophysics and Heat Transfer*, Vol. 12, No.4, pp. 543-551, 1998.

[18] Cook, W. J., and Felderman, E. J., "Reduction of Data from Thin Film Heat Transfer Gages: A Concise Numerical Technique," *AIAA Journal*, Vol. 4, No. 3, pp. 561-562, 1966.

[19] Ozisik, M. N., "Heat Conduction," John Wiley & Sons, Inc., 2nd, 1986.

[20] http://www.goodfellow.com

[21] White, K., Williams, A., and Nusca, M., "Plasma Output and Propellant Radiation Absorption Characteristics," Proceedings of 35th JANNAF Combustion Meeting, CPIA Publication 680, Vol. 1, pp. 237-246, December 1998.

[22] Nusca, M. J., McQuaid, M. J., and Anderson, W. R., "Development and Validation of a Multi-species Reacting Flow Model for the Plasma-jet Generated by an ETC Igniter," 37th JANNAF Combustion Meeting, Monterey, CA, November 2000.

[23] Kurabayashi, K., M. Asheghi, M. Touzelbaev, and K. E. Goodson, "Measurement of the Thermal Conductivity Anisotropy in Polyimide Films," *J. Microelectromechanical Systems*, Vol. 8, No. 2, 1999, pp. 180-191.

[24] CRC Handbook of Chemistry and Physics, Edited by D. R. Lide, CRC Press, 1997.

[25] Beyer, R. A., and Pesce-Rodriguez, R. A., "Experiments to Define Plasma-Propellant Interactions," *IEEE Transactions on Magnetics*. Vol. 39, No. 1, 2003, pp. 207-211.

[26] Pesce-Rodriguez, R. A., Beyer, R. A., Kinkennon, A. E., Del Guercio, M., Kaste, P. J. and Newberry, J. E., "In-Depth Chemistry in Plasma-Exposed M30 and JA2 Gun Propellants", U.S. Army Research Laboratory, ARL-TR-2505, Aberdeen Proving Ground, MD, June 2001.

[27] Taylor, M. J., "Ignition of Propellant by Metallic Vapour Deposition for an ETC Gun System," *Propellants, Explosives, Pyrotechnics*, Vol. 26, 2001, pp. 137-143.

[28] Koleczko, A., Ehrhardt, W., Kelzenberg, S., and Eisenreich, N., "Plasma Ignition and Combustion," *Propellants, Explosives, Pyrotechnics*, Vol. 26, 2001, pp. 75-83.

[29] Bourham, M. A., Gilligan, J. G., and Oberle, W. F., "Analysis of Solid Propellant Combustion Behavior under Electrothermal Plasma Injection for ETC Launchers," *IEEE Transactions on Magnetics*, Vol. 33, No. 1, 1997, pp. 278-283.